REVIEW

National Science Review
5: 159–182, 2018
doi: 10.1093/nsr/nwx154
Advance access publication 26 December 2017

PHYSICS

Special Topic: Metamaterials

Breaking the barriers: advances in acoustic functional materials

Hao Ge[1], Min Yang[2], Chu Ma[3], Ming-Hui Lu[1,4], Yan-Feng Chen[1,4,*], Nicholas Fang[3,*] and Ping Sheng[2,*]

[1]National Laboratory of Solid State Microstructures and Department of Materials Science and Engineering, College of Engineering and Applied Sciences, Nanjing University, Nanjing 210093, China; [2]Department of Physics, Hong Kong University of Science and Technology, Hong Kong, China; [3]Department of Mechanical Engineering, Massachusetts Institute of Technology, Cambridge, MA 02139, USA and [4]Collaborative Innovation Center of Advanced Microstructures, Nanjing University, Nanjing 210093, China

*Corresponding authors. E-mails: yfchen@nju.edu.cn; nicfang@mit.edu; sheng@ust.hk

Received 9 October 2017; **Revised** 11 December 2017; **Accepted** 11 December 2017

ABSTRACT

Acoustics is a classical field of study that has witnessed tremendous developments over the past 25 years. Driven by the novel acoustic effects underpinned by phononic crystals with periodic modulation of elastic building blocks in wavelength scale and acoustic metamaterials with localized resonant units in subwavelength scale, researchers in diverse disciplines of physics, mathematics, and engineering have pushed the boundary of possibilities beyond those long held as unbreakable limits. More recently, structure designs guided by the physics of graphene and topological electronic states of matter have further broadened the whole field of acoustic metamaterials by phenomena that reproduce the quantum effects classically. Use of active energy-gain components, directed by the parity–time reversal symmetry principle, has led to some previously unexpected wave characteristics. It is the intention of this review to trace historically these exciting developments, substantiated by brief accounts of the salient milestones. The latter can include, but are not limited to, zero/negative refraction, subwavelength imaging, sound cloaking, total sound absorption, metasurface and phase engineering, Dirac physics and topology-inspired acoustic engineering, non-Hermitian parity–time synthetic active metamaterials, and one-way propagation of sound waves. These developments may underpin the next generation of acoustic materials and devices, and offer new methods for sound manipulation, leading to exciting applications in noise reduction, imaging, sensing and navigation, as well as communications.

Keywords: acoustic metamaterials, phononic crystals, topological acoustics, PT-symmetry synthetic acoustics, sound absorption

INTRODUCTION

The study of acoustics involves the generation, propagation, detection and conversion of mechanical waves, i.e., sound and elastic waves. This classical field includes diverse sub-disciplines such as electroacoustics, architectural acoustics, medical ultrasonics, and underwater acoustics. Over the last three decades, the emergence of phononic crystals and acoustic metamaterials has provided us with new, powerful materials to manipulate sound and vibrations, owing to their anomalous acoustic dispersion relations and unusual properties originating from multiple scatterings in periodic structures, or local resonances of subwavelength unit cells. Many novel effects, such as subwavelength imaging, negative refraction, invisible cloaking and one-way sound transport became possible. Together with similar developments of photonic crystals and optical metamaterials, the field of classical waves has witnessed what is probably the most influential revolution over the past century. However, the origin of this revolution can be traced to the quantum theory of solids, with the advent of the theory of electronic bands.

Crystals are solid-state materials whose constituents are arranged periodically in space. In 1987, the concept of photonic crystals, an optical analogue of electronic crystals, was proposed by Eli Yablonovitch and Sajeev John [1,2], which opened a brand new field with great impacts for manipulating light. A similar concept for acoustics was also proposed in parallel to electromagnetism, known as phononic crystals [3,4]. The last two decades

have witnessed rapid developments in the field of phononic crystals [5–9]. Photonic and phononic crystals are both composed of periodically arranged scatterers in a homogeneous matrix. The periodic structures affect the propagation of optical and acoustic waves in a similar way to the atomic lattices interacting with the electronic waves. Waves of specific frequencies and momenta are allowed to propagate in the periodic system. These states are referred to as Bloch states and form an energy-band structure, which is defined in the reciprocal space (momentum space), denoted as the Brillouin zone. There may exist gaps separating different energy bands in the band structure. In the bandgaps, wave propagation is prohibited along certain, or all, directions. Early research on phononic crystals focused on the search for full band gap materials with exceptional sound attenuation [10,11]. Within the band gap, acoustic waves can be trapped at a point defect, or propagate along the line defect that can serve as a waveguide. Later, wave propagation in the pass band was extensively studied, and exotic properties, such as negative refraction, extraordinary transmission and acoustic collimation [12–14], were explored. These effects offered great potential for applications. More recently, the advent of graphene and its Dirac cones with linear dispersions have inspired the study and fabrication of phononic crystals with Dirac-quasiparticle-like behaviors that can experimentally reproduce quantum electronic phenomena such as Zitterbewegung and pseudo-diffusion transport of acoustic waves [15–17]. Also, topological phases of matter [18,19] and the attendant concept of geometry, i.e. topology, were transferred to the realm of photonics in 2005, and numerous theoretical and experimental investigations demonstrated the feasibility of topological photonic states [20,21]. Subsequently, topological properties in phonon transport were investigated, uncovering the relationship between the geometric phase and the phonon Hall conductivity [22–24]; topological phases were also realized in acoustic systems, drawing considerable attention [25–28].

In order for the phononic crystals to be effective in manipulating the acoustic waves, the lattice constants need to be comparable to the relevant wavelength. It follows that for low-frequency sound, the huge size of the phononic crystal makes it impractical. In 2000, a locally resonant material was proposed that exhibited band gaps with the lattice constant in the deep-subwavelength scale [29]. In contrast to the band gaps arising from Bragg scattering in phononic crystals, here the band gaps are induced by the local resonances of the structured unit cells. The building block of the locally resonant material is a solid sphere coated with soft silicone rubber and embedded into a hard matrix material. The building block can be described by a spring-mass model [30], with the solid sphere being the mass, connected to the rigid matrix by the soft silicone rubber, which acts like a spring. The spring allows relative motions between the mass and the rigid matrix. Near the resonance frequency, the central mass accelerates out of phase with respect to the applying force on the rigid matrix and the dynamic mass density of the block can turn negative [31]. The introduction of local resonances in a composite medium can have far-reaching consequences. The wave vector of an acoustic wave in a homogeneous medium is given by $k = |n|\omega/c$, with $n^2 = \rho/\kappa$. The mass density ρ and bulk modulus κ are the two key parameters of acoustic materials. If the effective mass density ρ is negative and the modulus κ is positive, then the wave vector k would be imaginary and the wave decays as it propagates, thereby giving rise to the band gaps of the locally resonant material. This is the first work utilizing local resonances of the subwavelength building blocks to achieve unusual acoustic material properties, and the field of acoustic metamaterials was initiated with very rapid subsequent development [32–35]. Resonance-induced negative effective bulk modulus and double-negative acoustic metamaterials were demonstrated theoretically and experimentally [36,37]. Acoustic metamaterials require no periodicity and can be designed at the deep-subwavelength scale. Hence they can be described by the effective medium theory [38–42]. Moreover, the concept of acoustic metamaterials is not limited only to the locally resonant materials or strictly periodic structures. In a broader sense, assemblies of subwavelength blocks with homogenized (over the wavelength scale) exotic acoustic properties and functionalities that do not exist in nature can be termed acoustic metamaterials.

Acoustic metamaterials that can display both positive and negative effective mass density and bulk modulus are the basis for realizing many intriguing functionalities. For example, reversed Doppler effects have been observed in double-negative materials [43]. Super-resolution imaging can be achieved by designing the flat lens made of double-negative materials [44]. Transformation acoustics and invisibility cloaking require anisotropic and spatially varying acoustic materials that can only be satisfied by acoustic metamaterials [45]. More recently, under the guidance of parity–time (PT) symmetry, acoustic metamaterials with adjustable loss and gain components have extended the modulation of the response parameter values to the complex domain, with unexpected consequences [46,47]. The extension of the response parameter values from the previously real, positive values to the complex domain has opened up unprecedented possibilities for wave manipulation.

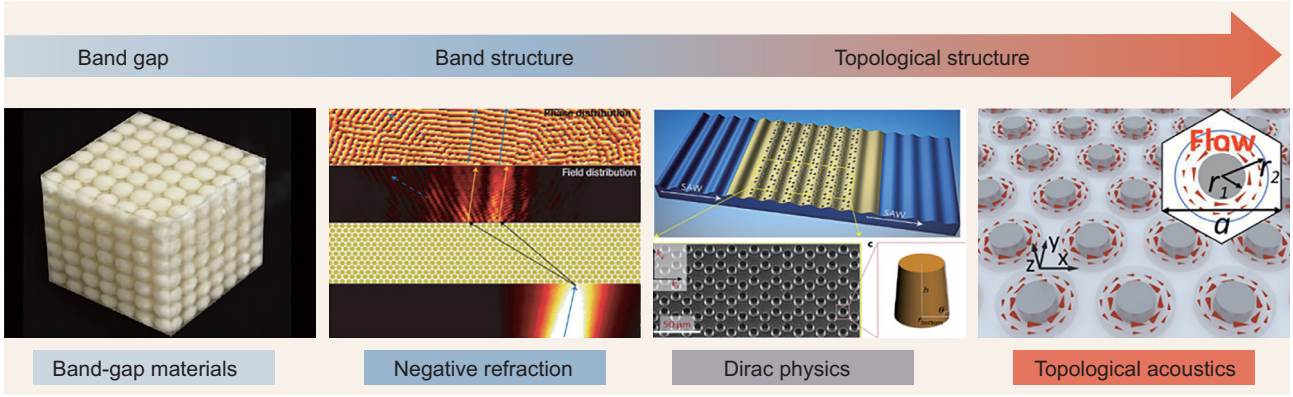

Figure 1. The roadmap for phononic crystals. At first, researchers focused on the band gap and band structures of phononic crystals. Nowadays, the topology of the wave functions has drawn considerable attention and the field of topological acoustics is rapidly developing. From left to right: adapted from [33]; adapted with permission from [56], Copyright 2007, Macmillan Publishers Ltd; adapted with permission from [17], Copyright 2016, Macmillan Publishers Ltd; adapted with permission from [25], Copyright 2015, American Physical Society.

In what follows, the first part of this review will explore the energy-band-related concepts and phenomena associated with phononic crystals (Fig. 1). Topological acoustics, as a new emerging field, is the latest addition to this area. In the second part, we focus on the unconventional effective properties of acoustic metamaterials and their diverse functionalities, including subwavelength imaging, invisibility cloaking, phase engineering, sound absorption and PT-symmetric acoustics, to name just a few.

PHONONIC CRYSTALS

Negative refraction in phononic crystals

In 1968, Veselago proposed the concept of left-hand material (LHM) with simultaneous negative electric permittivity and negative magnetic permeability [48]. In LHMs, the vectors of the electric field E, the magnetic field H, and wave vector k form a left-hand relationship, and the direction of propagation (the phase velocity) is opposite to the direction of energy flow (the group velocity). The refractive index of LHMs is negative and hence LHMs are also referred to as negative index materials (NIMs). Surprising wave propagation phenomena in LHMs, such as negative refraction, were theoretically predicted. Negative refraction means that the obliquely incident wave impinging on the interface will bend to the same side of the interface normal. Negative refraction of acoustic waves was first investigated in phononic crystals and then in acoustic NIMs. Unlike the NIMs, negative refraction in phononic crystals is caused by multiple Bragg scattering and strong deformation of isofrequency surfaces [49–51]. There exist two different mechanisms accounting for negative refraction in phononic crystals. The first case occurs in the lowest band due to the intense scattering near the Brillouin zone boundary and the incident and refracted waves stay on the same side of the interface normal [49,50]. However, the effective refractive index is not negative in this case and the phononic crystal behaves like a normal right-hand material. The other case occurs in the second or higher bands [51]. Due to the band-folding effect, the effective refractive index is negative and the wave vector is opposite to the energy flow, exhibiting a backward-wave negative refraction effect, which is similar to the NIMs. Negative refraction in phononic crystals can be used to focus a diverging wave into a focal point. The imaging effects with 2D and 3D phononic crystals were examined in several papers [52–55]. Negative birefraction of acoustic waves has also been reported in phononic crystals [56]. Unlike the birefringence phenomenon in optical materials, which is induced by the excitation of different polarization states, negative birefraction in phononic crystals is due to the excitation of two Bloch states simultaneously from the overlapping high energy bands. Two negative refractive directions corresponding to different states were shown in the simulation result and double-focusing of a point source was also experimentally observed.

Dirac physics and reproduction of quantum phenomena with classical waves

The Dirac equation, derived by one of the greatest physicists of the last century, Paul Dirac, successfully combines the theory of special relativity with quantum mechanics, and motivates the development of quantum field theory. The Dirac equation predicts a variety of intriguing effects of relativistic quantum particles, such as the Klein paradox and

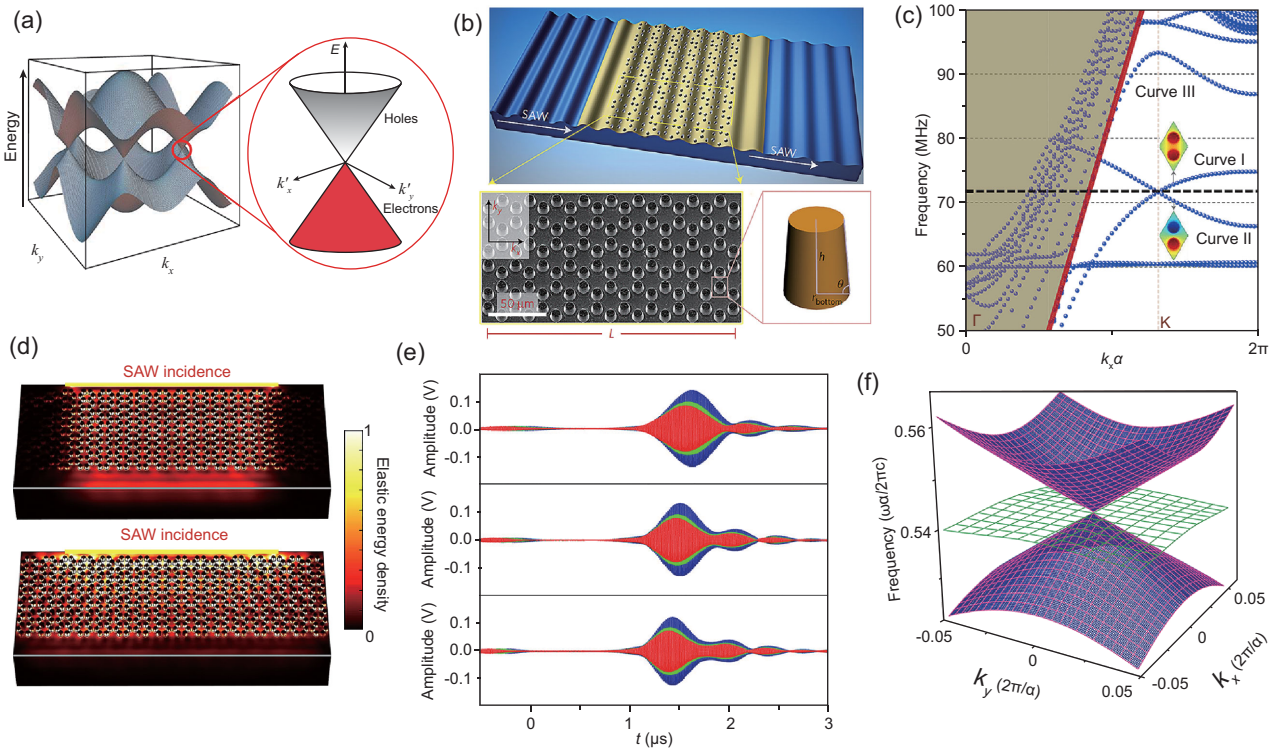

Figure 2. (a) The band structure of graphene, showing that the valence and conduction bands touch at the Dirac point. (b) The artificial surface phononic graphene on the $LiNbO_3$ substrate. (c) The calculated band structure of the surface phononic graphene. (d) The lower (upper) panel shows the elastic energy densities for the band region at (away from) the Dirac point. (e) Temporal transmission spectra of the Gaussian pulse with different bandwidths. (f) The Dirac-like cone at the center of the Brillouin zone. Two linear bands and an additional flat band intersect at the Dirac point. (a) adapted from [59]; (b)–(e) adapted with permission from [17], Copyright 2016, Macmillan Publishers Ltd; (f) adapted with permission from [72], Copyright 2011, Macmillan Publishers Ltd.

Zitterbewegung. However, these effects are extremely difficult to be directly observed in real relativistic quantum particles. In an alternative way, researchers start seeking experimental platforms in condensed matter physics to simulate these relativistic quantum effects under the same mathematical model [57], and the 2D material, graphene, considered as a good candidate, has been extensively studied [58–60]. Due to the honeycomb lattice symmetry of graphene, a conical singularity determinately appears at the corner of the Brillouin zone (Fig. 2a), referred to as a Dirac point. Near the Dirac point, the dispersion depends linearly on the wave vector, and the dynamics of electrons can be described by the massless Dirac equation. The system of classical waves can also have Dirac points, and hence Dirac-physics-related phenomena. Dirac points at the Brillouin zone boundary have been found in photonic and phononic crystals with honeycomb lattice [61–63] and many novel effects, such as pseudo-diffusion transport and Zitterbewegung, have been experimentally observed [15–17,64]. Compared with graphene, these artificial graphene systems have great advantages in flexible designing and high-fidelity measurements for quantum simulation of the Dirac equation. Here, we briefly introduce an artificial surface phononic graphene [17], which utilizes the surface acoustic wave (SAW) system to construct on-chip artificial graphene. SAW is an acoustic wave traveling along the surface of solids and decaying exponentially with depth into the substrate. By incorporating a metallic micro-pillar array of honeycomb lattice on the surface of the $LiNbO_3$ substrate (Fig. 2b), a periodic potential variation is introduced to the SAW and Dirac cone dispersion can be observed in the calculated band structure (Fig. 2c). A transmission dip appeared around the Dirac point frequency in the measured SAW transmission spectrum, indicating the pseudo-diffusion effect, which is related to the singularity in the dispersion relation. The diffusion behavior of the energy flux was revealed by the simulation result at the Dirac point frequency, showing that the SAW field spreads out immediately inside the phononic crystal, which is different from the ballistic transport in band regions away from the Dirac point (Fig. 2d). A specific characteristic of the diffusion transport is that the product of the transmission coefficient and the sample thickness in the propagation direction (*TL* product) is a constant, while the *TL* product of the

ballistic transport grows linearly with the sample thickness. By measuring the transmittance through samples with growing numbers of unit cells in the propagation direction, the nearly constant *TL* product confirmed the occurrence of the pseudo-diffusion transport. The dynamic behavior of a Gaussian pulse with a center frequency at the Dirac point was also measured. The transmitted signal exhibited strong temporal oscillations and the beating strength decayed exponentially with time (Fig. 2e), which can be regarded as an acoustic analogue of the Zitterbewegung effect. The beating effect originates from the interference between two Bloch states locating at each side of the Dirac point, similar to the interference between the positive and negative energy states in relativistic quantum physics. Besides these intriguing effects mentioned above, as a 2D system, various surface manipulations of SAW transportation properties are enabled; for instance, an artificial gauge field can be constructed by strain engineering in the surface to explore topological physics [65]. This SAW platform is an ideal and low-cost candidate for studying Dirac physics, which in turn may help to improve the RF signal-processing abilities of SAW devices.

The Dirac cone dispersion can also be connected to zero-refractive-index materials, which seems apparently unrelated. Zero-refractive-index materials were first investigated by Engheta *et al.* [66,67] and then realized in acoustic systems [68–71]. The propagating waves experience zero phase change inside the zero-refractive-index materials and can squeeze through bending or narrow channels. The phase distribution is uniform inside such materials and thereby the shape of the transmitted wavefront is determined by the output boundary. Acoustic lenses can be achieved by designing boundaries with concave shapes. Photonic and phononic crystals with Dirac-like cone dispersions at the center of the Brillouin zone can exhibit zero-refractive-index behaviors [72,73]. The Dirac-like cone is induced by the accidental degeneracy of the monopolar and dipolar modes in a square lattice, showing that two linear bands and an additional flat band intersect at the Dirac point (Fig. 2f). The term 'accidental' means that the degeneracy is not supported by the crystal symmetry; instead, it can only be formed under specific system parameters. By applying the effective medium theory, it is shown that the effective permittivity ε_{eff} and permeability μ_{eff} of the photonic crystal or the effective mass density ρ_{eff} and reciprocal of bulk modulus $1/\kappa_{\text{eff}}$ of the phononic crystal approach zero simultaneously at the Dirac point frequency, leading to the zero refractive index. The double-zero constitutive parameters also ensure that the effective impedance is finite and high transmission is permitted. A critical requirement for the zero refractive index here is that the phase velocity in the periodic scatters needs to be lower than in the host medium, which is difficult to realize in airborne sound systems where air serves as the host medium with ultra-low sound velocity. A feasible design was proposed by designing periodic cylindrical air columns that are higher than the background air in a 2D waveguide [74]. The sound speed in the air columns (the scatters) for the first-order waveguide mode is lower than in the waveguide (the host medium), which satisfies the requirement. Collimation of sound from a point source was observed and the Dirac-like cone dispersion was directly measured by probing the sound field inside the waveguide.

Moreover, Dirac physics plays an important role in the field of topological materials. Topological transition between topologically distinctive phases takes place when the band gap closes and reopens. The critical transition point corresponds to a gapless energy spectrum with a point degeneracy, which often emerges as a Dirac point. In the realm of topological photonic and phononic crystals, the common procedure is first to obtain a Dirac degeneracy, and then to lift the degeneracy by breaking certain symmetries to form topological nontrivial states [20,21]. The Dirac equation is also the key to topological states, and, generally speaking, each topological state is governed by a Dirac or Dirac-like equation [75].

Topological acoustics

Topology is a mathematical concept concerned with the properties of space that are invariant under continuous perturbations. A simple example to introduce topology is that a doughnut can be continuously deformed and reshaped into a coffee mug without tearing or gluing; however, a sphere cannot. The reason is simple, as the coffee mug and doughnut both have a hole inside, while the sphere does not, and the hole cannot be simply annihilated or generated under continuous deformations. Now we can use the number of holes to group these objects into different categories. The number of holes, corresponding to the value of genus (g), can be considered as a topological invariant. Objects with the same topological invariant are topologically equivalent. The genus is defined by the Gauss–Bonnet theorem, as the surface integral of Gaussian curvature (K) over the object:

$$2\,(1-g) = \int_{\text{surface}} K dA/(2\pi) \qquad (1)$$

It is a globally defined discrete integer and is insensitive to locally continuous small perturbations.

In 1980, von Klitzing discovered that, at low temperature and under strong magnetic field, the Hall conductance of the 2D electron gas takes quantized values as ne^2/h (h is the Plank constant and e is the electron's charge) and is independent of sample size and unaffected by impurities [76]. Moreover, while the bulk behaves like an insulator, there exist chiral edge states moving along the edge at one direction without backscattering or dissipation. This effect, known as the integer quantum Hall effect, uncovered the existence of distinctive phases of matter, called topological phases, which cannot be described by the theory of spontaneous symmetry breaking. Over the last three decades, this area has become an active field and numerous topological phases have been discovered theoretically and experimentally, including the quantum anomalous Hall effect, topological insulators, Weyl semimetals and topological superconductors, which could have promising applications in next-generation electronic devices and topological quantum computation. These intriguing new effects and distinctive phases of matter are actually related to the topological structures of the electronic wave functions in the reciprocal space (or momentum–energy space), and can be described and classified by a quantized topological invariant, such as the Chern number (or the Thouless-Kohmoto-Nightingale-den Nijs (TKNN) invariant), which is the integral of Berry curvature over the reciprocal space. The integer n in the Hall conductance of the quantum Hall effect actually corresponds to the Chern number, first revealed by David J. Thouless *et al.* [77]. Similar to the genus as a topological invariant in geometry, the Chern number characterizes the global behaviors of the electronic wave functions and cannot change when the system varies smoothly without closing the band gap, which explains the robust behaviors of topological materials. The Chern number only changes discretely when phase transition occurs; meanwhile the band gap closes and reopens, and the topological structure of the wave functions changes. At the interface between two topologically inequivalent materials, the different Chern numbers need to be neutralized and a phase transition must occur. As a result, the band gap vanishes at the interface and there exist gapless conducting edge states. These edge states are guaranteed by the topological properties of the insulating bulk energy bands and are insensitive to impurities and perturbations because there are no available states for backward propagation. The chiral edge states in the integer quantum Hall effect mentioned above locate at the interface between the integer quantum Hall state and the vacuum. The integer quantum Hall state corresponds to a nontrivial insulator with nonzero Chern number while the vacuum can be considered as a trivial insulator with zero Chern number. The chiral edge states actually originate from the difference in topological invariants between these two systems.

The Chern number for the nth band is defined as the total Berry flux in the Brillouin zone:

$$C_n = \frac{1}{2\pi}\oiint F(\mathbf{k})\cdot ds, \tag{2}$$

where $F(\mathbf{k}) = \nabla_{\mathbf{k}} \times A(\mathbf{k})$ is the Berry curvature, and $A(\mathbf{k}) = \langle u_n(\mathbf{k})|i\nabla_{\mathbf{k}}|u_n(\mathbf{k})\rangle$ denotes the Berry connection. The geometric phase, known as the Berry phase, is the integral of the Berry connection along a closed loop. $|u_n(\mathbf{k})\rangle$ represents the Bloch state with momentum $\mathbf{k}$ in the nth band. The integral is carried out over the entire 2D Brillouin zone. The Berry curvature is even under parity (P) symmetry, as $F(\mathbf{k}) = F(-\mathbf{k})$, and odd under time-reversal (T) symmetry, as $F(\mathbf{k}) = -F(-\mathbf{k})$. In the presence of T symmetry, the integral of Berry curvature over the entire Brillouin zone is zero, which results in a zero Chern number. In order to acquire a nonzero Chern number, the T symmetry needs to be broken, while the P symmetry is preserved.

The distinctive properties of topological phases originate from the nontrivial band topologies, and naturally, these concepts can be transferred to the realm of photonic and phononic crystals. An analogue of the quantum Hall effect was first realized in gyromagnetic photonic crystals by applying a magnetic field on the gyromagnetic material to break the time-reversal symmetry at microwave frequencies [78,79]. A one-way topologically protected edge mode was observed and exhibited robust transport against defects and bends. However, it is difficult to break the time-reversal symmetry in acoustic systems; this is usually achieved by utilizing the magneto-acoustic effect or nonlinear materials [80]. The magneto-acoustic effect is weak for longitudinal acoustic waves in fluids and the low efficiency and instability of nonlinear material restrict its application. A feasible method was proposed by Fleury *et al.* by applying moving air flow in a ring-shaped resonator [81]. Similar to the way that circulating electrons produce a magnetic field, the circulating flow produces an acoustic analogue of a magnetic field for sound and splits the degeneracy of the counter-propagating modes, which can be regarded as an analogue of the Zeeman effect. The simplified wave equation for sound propagating in the circulating air flow can be expressed as [82]:

$$[(\nabla - i\vec{A}_{\text{eff}})^2 + \omega^2/c^2 + (\nabla\rho/2\rho)^2 - \nabla^2\rho/(2\rho)]\phi = 0 \tag{3}$$

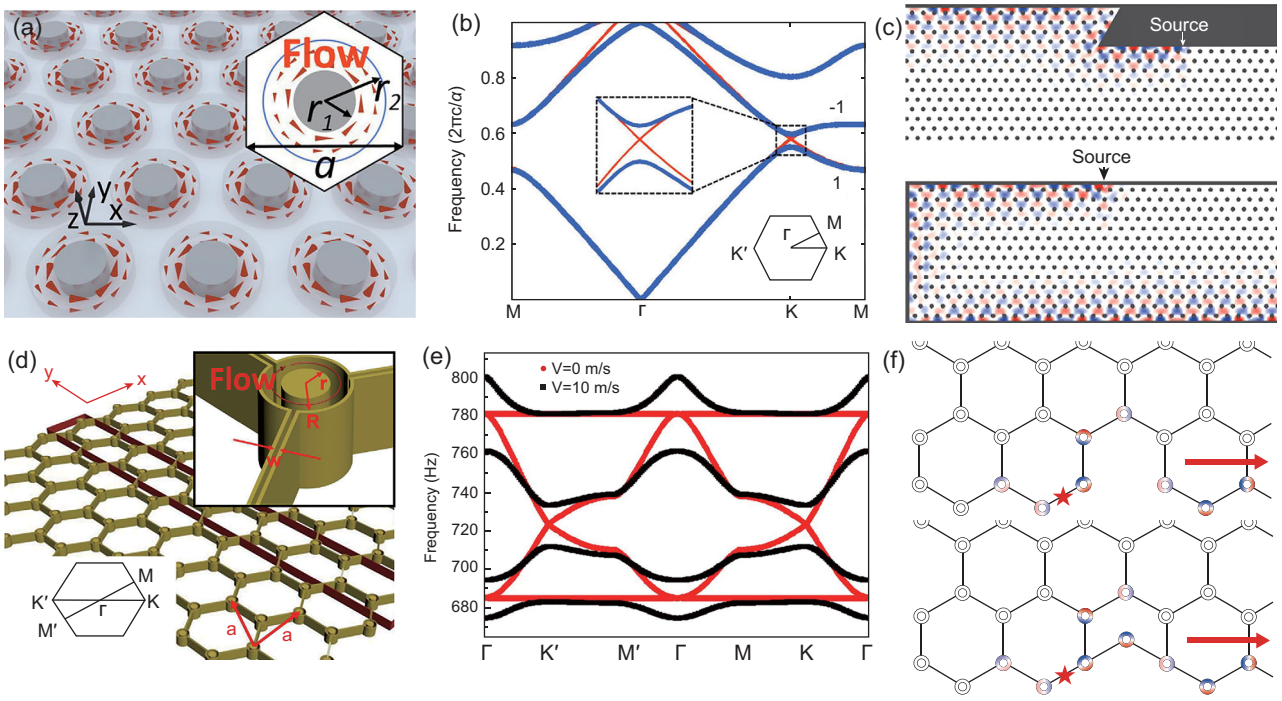

Figure 3. *T*-broken triangular (a) and honeycomb (d) lattice phononic crystals by incorporating the circulating flow. In (b) and (e), the red lines represent the band structures without flow. After introducing the circulating flow, the degenerate points are all lifted. (c), (f) One-way edge states at the boundary that are immune to defects and bends. (a)–(c) adapted with permission from [25], Copyright 2015, American Physical Society; (d)–(f) adapted from [82].

where ϕ is the velocity potential and c and ρ are the sound velocity and mass density of air. The term $(\nabla\rho/2\rho)^2 - \nabla^2\rho/(2\rho)$ denotes the scalar potential, and $\vec{A}_{\text{eff}} = -\omega|\vec{V}|\vec{e}_\theta/c^2$ represents the effective vector potential, with V and $\vec{e}_\theta$ being the amplitude and azimuthal unit vector of the circulating flow velocity. An effective 'magnetic field' for sound $\vec{B}_{\text{eff}} = \nabla \times \vec{A}_{\text{eff}}$ emerges and breaks the time-reversal symmetry. Now we can construct *T*-broken triangular (Fig. 3a) or honeycomb (Fig. 3d) lattice phononic crystals by incorporating the circulating flow into the ring-shaped unit cells [25,82–84]. Due to the lattice symmetry, a pair of Dirac points will determinately appear at the corners of the Brillouin zone without the flow. Besides, for the honeycomb lattice phononic crystal, there exist two quadratic degenerate points at the center of the Brillouin zone. When the circulating flow is introduced, the time-reversal symmetry is broken. The degeneracies of the Dirac points and quadratic degenerate points will all be lifted (Fig. 3b, e), and the neighbor energy bands acquire nonzero Chern numbers, which means that the phononic crystal is in a nontrivial topological phase. The gapless edge state is demonstrated by putting a rigid wall, considered as a topologically trivial insulator for sound, at the boundary of the topological phononic crystal. The number of edge states is equal to the difference between the gap Chern numbers of two phases, where the gap Chern number is defined as the sum of the Chern numbers of all the bands below the band gap, which is equal to plus (minus) one for the triangular (honeycomb) phononic crystal, and zero for the rigid wall here. As a result, there exists one chiral edge state at the boundary of the phononic crystal. The propagation direction of the edge state is determined by the sign of the difference between the gap Chern numbers of two phases. The edge state exhibits unidirectional propagation along the interface and immunity to various types of defects, showing a topologically protected robust sound transport (Fig. 3c, f).

Time-dependent modulation has also been introduced to break the time-reversal symmetry [85] and realize an effective magnetic field [86]. A time-modulated hexagonal lattice phononic crystal composed of coupled acoustic trimers was recently proposed [87], as an acoustic analogue of the Floquet topological insulator. Each trimer contains three acoustic cavities connected by waveguides, and the acoustic capacitance of each cavity is modulated by a periodic potential $\Delta C_m(t) = \delta C \cos(\omega_m t - \varphi_m)$. The phase φ_m changes along the clockwise direction inside the trimer, with a phase difference of $2\pi/3$ between two adjacent cavities, producing a rotating modulation effect. This spatiotemporal modulation breaks the time-reversal symmetry, and thus a topologically nontrivial phase emerges.

Unidirectional edge states immune to structural defects were also demonstrated.

Employing time-dependent modulation and circulating fluids are both technically challenging. For ease of implementation, it is more practical to explore an acoustic topological phase with preserved time-reversal symmetry. The quantum spin Hall effect (or the topological insulator) can be induced by the strong spin–orbit interactions and protected by the time-reversal symmetry [18,19]. There exist counter-propagating spin-locked edge states in the band gap and the gapless edge dispersion is guaranteed by the Kramers degeneracies at the time-reversal invariant momentum points. However, an acoustic analogue of the quantum spin Hall effect is not straightforward due to the difference in the time-reversal operators between fermionic and bosonic systems. For fermions with half-integer spin, such as electrons, the time-reversal operator T_f satisfies ${T_f}^2 = -1$, and hence enables the Kramers doublet, which is critical for the quantum spin Hall effect. However, for bosons with integer spin, such as phonons, the time-reversal operator T_b satisfies ${T_b}^2 = 1$, which is quite different. It is necessary to construct fermion-like pseudo time-reversal symmetry and pseudo-spin states to realize the quantum spin Hall effect and topological insulator in bosonic systems [88]. Although photons do not possess the same spin-1/2 characteristic as electrons, two polarizations of photons can be utilized to construct polarization-based pseudo-spin states and form the Kramers doublet [89]. For acoustic waves in fluids, however, neither intrinsic spin-1/2 characteristics nor extra polarizations can be utilized to realize the acoustic analogue of the quantum spin Hall effect. It is necessary to explore new degrees of freedom for acoustic waves. Recently, a new scheme was proposed by using two pairs of degenerate Bloch modes to construct photonic pseudo-spin states in dielectric materials [90], which paves the way for realizing the acoustic analogue of the quantum spin Hall effect [28,91–94]. For acoustic systems, double Dirac cones (four-fold degeneracy) can be accidentally formed at the Brillouin center by adjusting the filling ratio of the honeycomb lattice [95] or the triangular lattice with core-shell structures [96], or formed by the zone-folding mechanism [90]. Here, we discuss the accidentally formed case in the honeycomb lattice. The accidental four-fold degeneracy is composed of two degenerate dipolar modes p_x/p_y and two degenerate quadrupolar modes $d_{x^2-y^2}/d_{xy}$, which are related to the 2D irreducible representations of C_{6v} symmetry. At higher or lower filling ratios, these two pairs of degenerate modes will be separated by a band gap. These two-fold degenerate modes can be hybridized to construct the pseudo-spins for the bulk states as $p_\pm = (p_x \pm i\,p_y)/\sqrt{2}$ and $d_\pm = (d_{x^2-y^2} \pm i\,d_{xy})/\sqrt{2}$, and the angular momenta of wave functions play the role of pseudo-spins [28]. The corresponding pseudo time-reversal operator T_p is constituted by the complex conjugate operator and the rotational operator related to the C_{6v} symmetry. The T_p operator is fermion-like (${T_p}^2 = -1$) and thus enables the Kramers doublet. With the filling ratio of the honeycomb lattice continuously decreasing from a large ratio, the band gap separating the two pairs of degenerate modes closes and reopens. During this process, band inversion occurs (the dipolar modes and quadrupolar modes exchange their positions) accompanied by a topological transition from a trivial phase to a nontrivial phase near the double Dirac cone (Fig. 4a), indicating an analogue of the quantum spin Hall effect. A pair of counter-propagating spin-locked edge states localize at the interface between the trivial and nontrivial phases, which are hybridized by the symmetric mode S and antisymmetric mode A at the interface as $S + i\,A/S - i\,A$. Propagation of the edge state is immune to various defects, such as cavities, bends and disorders (Fig. 4a), protected by the pseudo time-reversal symmetry. However, as the C_{6v} symmetry is not preserved at the interface, the counter-propagating pseudo-spin states will be slightly mixed and a tiny gap exists at the center of the Brillouin zone. This tiny gap could be reduced by optimally modifying the structure of the interface. Utilizing a cross-waveguide splitter, the spin-dependent transport was also verified by separating different pseudo-spin states in space (Fig. 4b).

Acoustic pseudo-spins have also been constructed in coupled ring resonators, corresponding to the clockwise and anticlockwise propagation modes. An anomalous Floquet topological insulator for sound was recently demonstrated by utilizing coupled anisotropic metamaterial rings, and spin-locked edge states were experimentally observed [97]. Topological engineering for underwater sound based on coupled rings has also been reported [98]. The acoustic edge states and an acoustic anomalous Floquet topological insulator was also experimentally demonstrated in an acoustic waveguide network [99]. The simple structure and high-energy throughput in the acoustic waveguide network leads to efficient and robust topologically protected sound propagation along the boundary.

Another type of pseudo-spin, named valley pseudo-spin, which utilizes the valley degree of freedom (local energy extrema of the energy bands), was also realized in phononic crystals [100]. By introducing a mirror-symmetry breaking, the Dirac degeneracies in the triangular lattice are

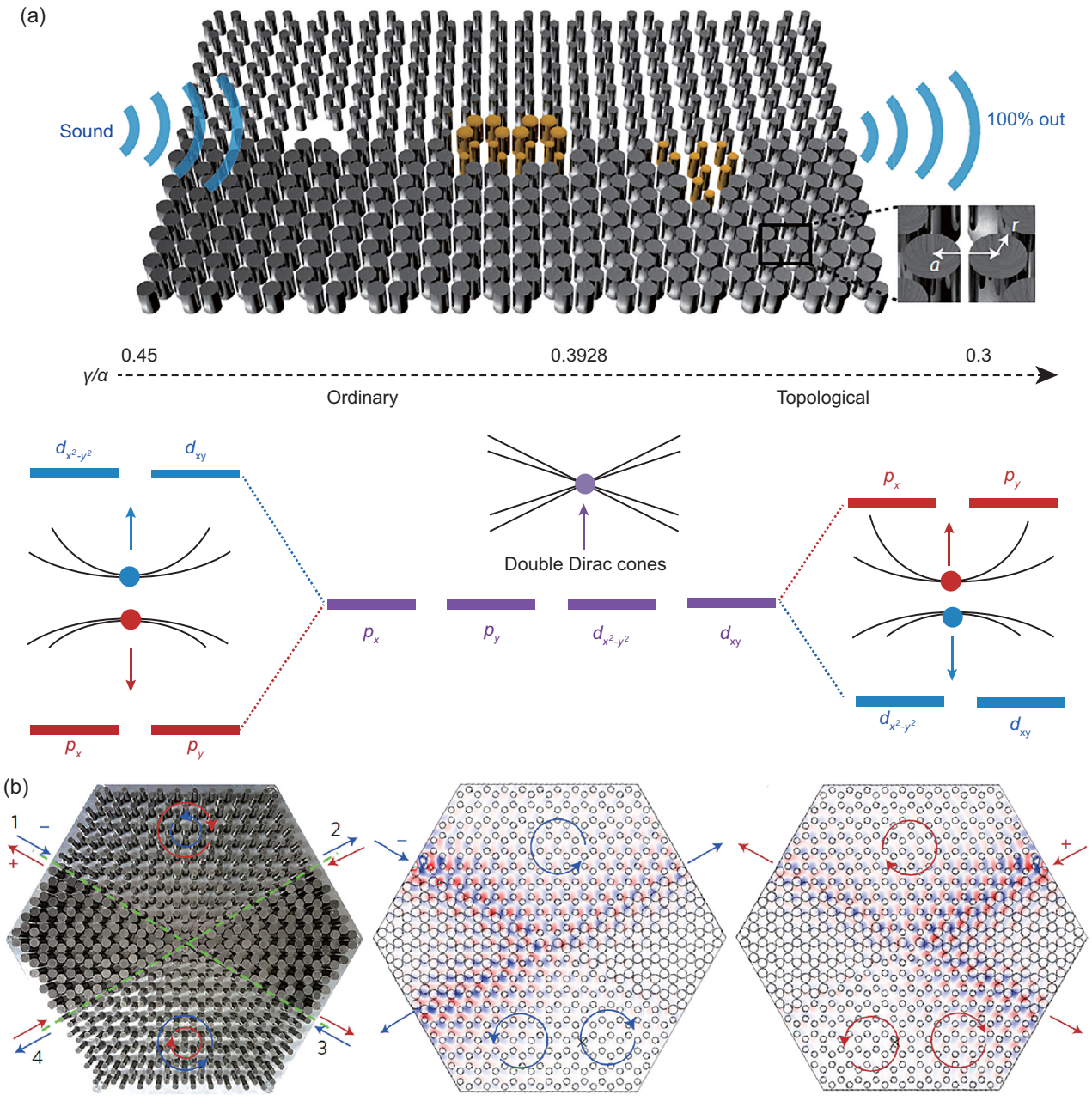

Figure 4. (a) The band inversion effect occurs near the double Dirac cones, accompanied by a topological phase transition. The edge states at the interface are robust against various types of defects. (b) Clockwise (anticlockwise) circulating propagation of the spin-up (-down) states in the cross-waveguide splitter. (a) and (b) adapted with permission from [28], Copyright 2016, Macmillan Publishers Ltd.

lifted and a valley Hall phase transition occurs. A pair of counter-propagating valley–chiral edge states localize at the interface between topologically distinct phases. Due to absence of inter-valley coupling, the edge states can pass through a sharply curved interface without backscattering. The edge states can also be selectively excited according to the angular selection rule. Experimental observation of valley–chiral edge states in an elastic hexagonal lattice has also been reported recently [101].

So far, we have mainly focused on 2D topological acoustic systems. The geometric phase in 1D systems, known as the Zak phase, was determined in a 1D phononic crystal [26]. Topological transition and high-density interface states were both experimentally demonstrated. The Weyl point, a linearly degenerate point in 3D momentum space, can be viewed as the monopole of the Berry flux [102]. Weyl points are robust and can only be annihilated in pairs with opposite charges. In acoustics, Weyl

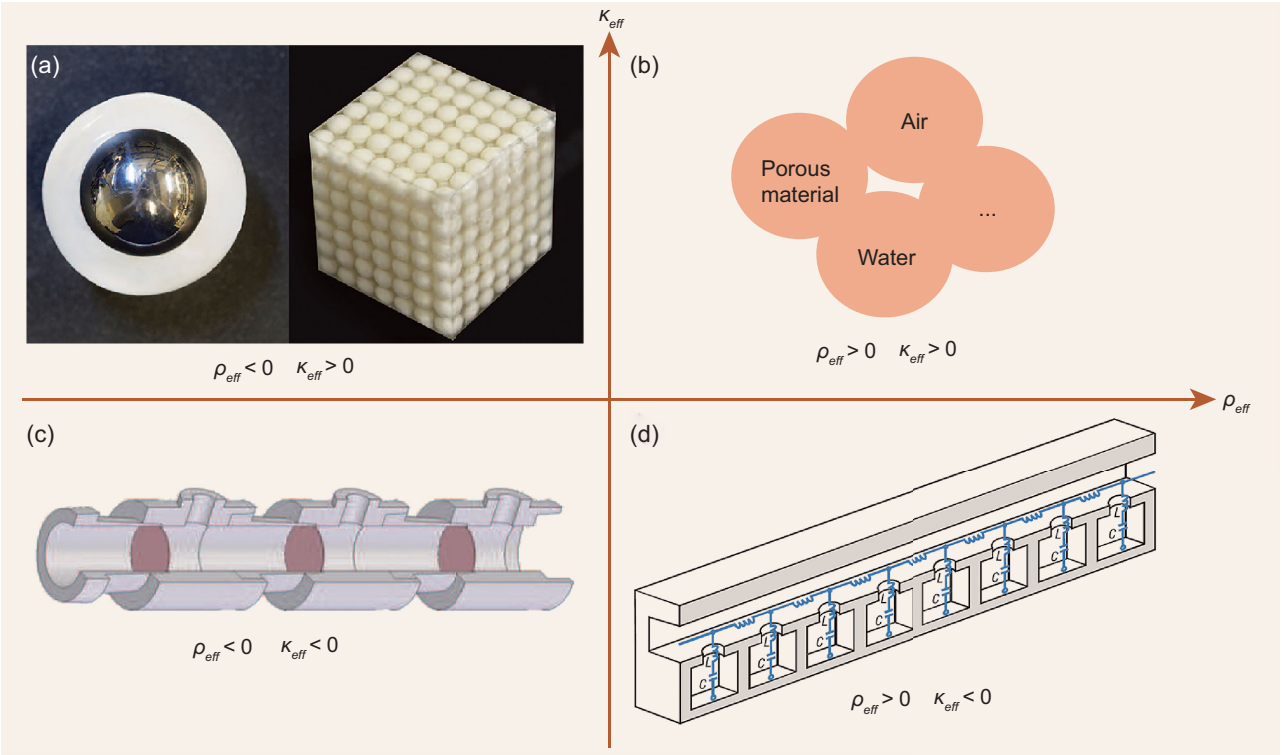

Figure 5. The parameter space for the mass density and bulk modulus. The effective density and modulus of acoustic metamaterials can display both positive and negative values due to the local resonances of the subwavelength structured unit cells. (a) adapted from [33]; (c) adapted with permission from [113], Copyright 2010, American Physical Society; (d) adapted with permission from [37], Copyright 2006, Macmillan Publishers Ltd.

points were first realized by incorporating chiral interlayer couplings or unequal onsite couplings in the staked honeycomb lattice [27,103]. A plane cut with a fixed k_z in the 3D Brillouin zone could acquire net Berry flux due to the existence of the Weyl point, resulting in a nonzero Chern number. A nonzero Chern number implies that there exist topologically protected chiral edge states at the interface between the system and the hard boundary. An acoustic type-II Weyl point was also realized by delicately stacking 1D dimerized chains and constructing a type-II Weyl Hamiltonian [104]. The type-II Weyl system exhibits a tilted cone-like spectrum and the existence of acoustic Fermi arcs was demonstrated by tracing the trajectories of the surface states at a fixed frequency. As a new emerging field, topological acoustics are still to be further investigated and explored. Acoustic analogues of the 3D topological insulators have not been realized as yet [105]. Phonon interactions can be introduced by utilizing nonlinear materials; hence, acoustic topological states and quasiparticles in correlated systems can be considered. Recently, topological phases in non-Hermitian systems have also attracted much attention and exhibit distinctive behaviors [106,107]. Non-Hermitian acoustic systems have been constructed in several designs and it is possible to introduce topological phases into these systems. Acoustic systems provide a superior platform for studying topological physics and its extensive ramifications, which in turn leads to a fascinating way to manipulate acoustic waves.

ACOUSTIC METAMATERIALS

Negative effective parameters in acoustic metamaterials

The mass density and bulk modulus are two key parameters of acoustic materials. Traditionally, for composites these two parameters are both positive and restricted by their constituents' parameters (Fig. 5b). In acoustic metamaterials, due to local resonances of subwavelength structured unit cells, the dynamic mass density and bulk modulus can exhibit strong frequency-dispersive properties and achieve effective negative values near the resonance frequencies. As mentioned in the introduction, the dynamic effective mass density of the locally resonant building block (Fig. 5a) is negative due to the relative out-of-phase motions between the center mass and the host matrix material near the resonance frequency. This type of resonance is defined as a dipolar resonance, which displays asymmet-

ric motions and modulates the mass density [36]. Similar dipolar resonances also exist in decorated membrane resonators (DMRs) [108], where a rigid platelet is attached to a flexible thin membrane with a fixed boundary. The thin DMR structure can totally block the low-frequency sound (which is usually difficult to be blocked according to the mass density law) at the anti-resonance frequency, between two neighboring resonance frequencies, where the dynamic mass density displays a strong dispersion with large positive and negative values. An array of thin membranes has also proved to be capable of exhibiting negative mass density below a critical frequency [109,110]. Another type of resonance, the monopolar resonance, is related to symmetric compressive/expansive motion, and can modulate the effective bulk modulus. In the case of soft rubber spheres suspended in water [36], the volume dilation of the rubber sphere could be out of phase with the applied pressure field near the monopolar resonance frequency, showing that the rubber dynamically expands under compression or compresses under stretching; hence, the effective bulk modulus turns out to be negative. Metamaterial with negative bulk modulus was first experimentally realized by utilizing a waveguide channel attached with an array of subwavelength Helmholtz resonators (HRs), as shown in Fig. 5d [37]. The HR is a rigid cavity with a narrow neck connected to the waveguide channel. Due to the collective resonances of the attached HRs, the volume dilation of the fluid segment in the waveguide is out of phase with the driving pressure field and the effective bulk modulus becomes negative. A similar design was later proposed, which consists of an array of side openings on a tube [111]. The effective bulk modulus is negative for a wide frequency range, extending from a certain cutoff frequency down to zero frequency.

As mentioned in the section entitled 'Negative refraction in phononic crystals', materials with double-negative constitutive parameters are denoted as NIMs. NIMs have been exploited to realize acoustic superlenses for subwavelength imaging, which will be discussed in the next section. NIMs can be constructed by combining two structures having negative mass density and negative bulk modulus separately, or utilizing just one resonant structure exhibiting both monopolar and dipolar resonances in an overlapping frequency range [112–116]. For example, a waveguide consisting of an array of interspaced membranes and side openings (Fig. 5c) can have simultaneously negative density and bulk modulus [113]. Recently, a 3D isotropic double-negative material was experimentally realized by utilizing soft macro porous microbeads [116]. The soft microbeads suspended in water can be considered as ultra-slow Mie resonators and exhibit strong monopolar and dipolar resonances in an overlapping frequency range, thus producing double negativity. Coupled DMRs can also achieve double negativity by adjusting the eigenfrequencies of the dipolar and monopolar resonances independently to make them overlap in a desired frequency range [115]. Unlike the resonance-based approaches, space-coiling structures can also exhibit a negative refractive index in a broad frequency range due to the geometric-induced band-folding effect [117].

Subwavelength imaging

Subwavelength imaging could have important applications in medical ultrasonic diagnostics, nondestructive evaluation and photoacoustic imaging. The resolution of conventional imaging devices is restricted by the diffraction limit, which arises from the loss of subwavelength details contained in the evanescent waves, which decay exponentially away from the object (or image), but carry large lateral wave vectors. This can be seen from the dispersion in a homogeneous medium $k^2 = k_\perp^2 + k_\parallel^2 = (2\pi/\lambda)^2$ (see Fig. 6a); if the lateral wave vector $k_\parallel$ exceeds $2\pi/\lambda$, where λ denotes the wavelength, the wave vector $k_\perp$ in the longitudinal direction must be imaginary. Hence the wave decays exponentially away from the source. Acoustic waves scattered from an object comprise both propagating waves and evanescent waves. To overcome the diffraction limit, the evanescent waves need to be transmitted and collected before they become too weak to be detected. There exist two feasible approaches: one is amplifying the evanescent waves and then capturing them in the near field, while the other is through providing extra wave vectors in the adjacent medium to sustain the evanescent waves, or converting them into propagating waves.

The first approach is the basis of the so-called superlens [118–120], first explored in optics by John Pendry, who observed that the evanescent waves can be strongly amplified inside the NIM [118]. After leaving the NIM, the evanescent waves decay and reconstitute in the image plane, thereby contributing to perfect imaging. This mechanism also applies to acoustic waves. Although resonance-induced material loss limits the performance of acoustic superlenses, promising results have been achieved [44,121,122]. Recently, a negative index acoustic superlens composed of HRs (soda cans) was experimentally demonstrated [44]. Generally, the HRs only create monopolar resonances and contribute to a singly negative parameter that is the negative effective bulk modulus. However, by breaking the

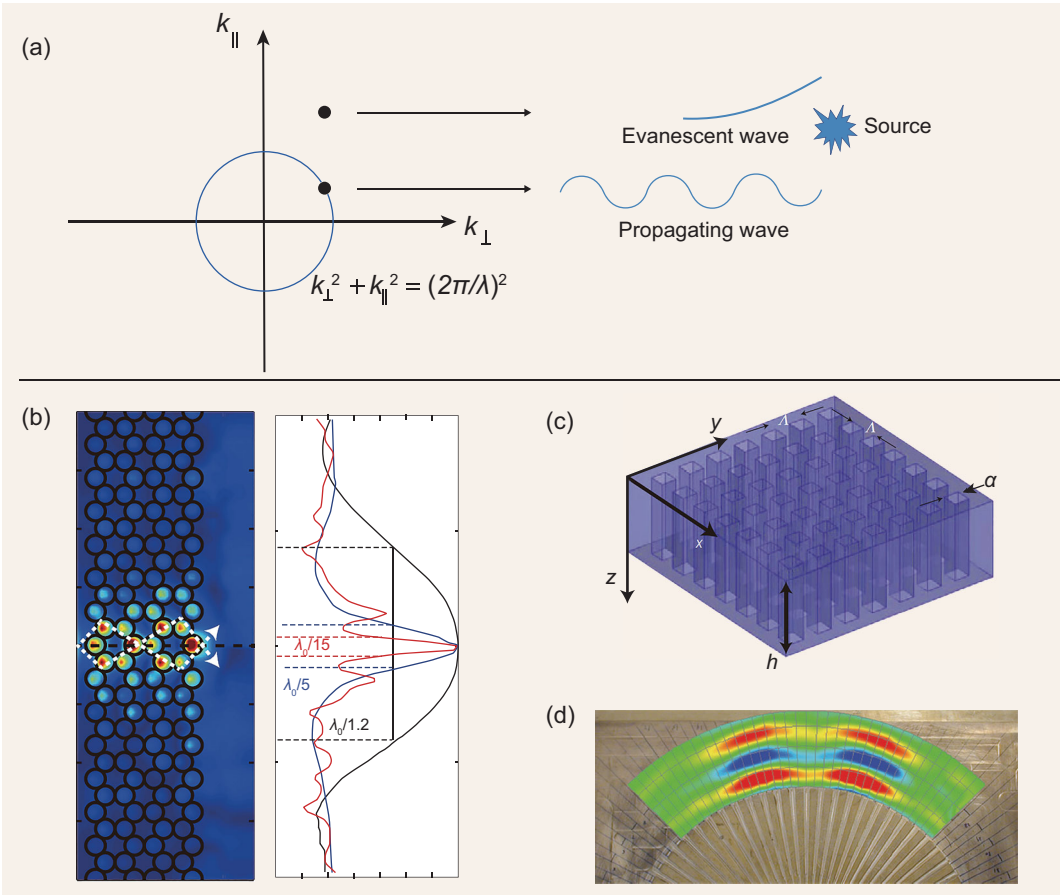

Figure 6. (a) The wave vector is constrained by the dispersion relation. The modes outside of the circle correspond to the evanescent waves. (b) The negative index acoustic superlens is composed of a honeycomb array of identical Helmholtz resonators. An image with a 1/15 wavelength width at half-maximum can be observed in the near field. (c) The holey structure with periodic subwavelength apertures can support Fabry–Pérot resonant modes. (d) The acoustic hyperlens is composed of alternating air and brass layers. The evanescent waves will be gradually converted into propagating waves and then observed in the far field. (b) adapted with permission from [44], Copyright 2015, Macmillan Publishers Ltd; (c) adapted with permission from [125], Copyright 2010, Macmillan Publishers Ltd; (d) adapted with permission from [128], Copyright 2009, Macmillan Publishers Ltd.

symmetry and forming a bi-period honeycomb lattice with two resonators in a unit cell, a narrow band that presents a negative refractive index emerges in the band gap, which is induced by the multiple scatterings between the two resonators. The subwavelength imaging effect was verified in this negative index acoustic superlens, with a focal spot that is seven times better than the diffraction limit (Fig. 6b). Negative index is not the necessary condition for amplification of acoustic evanescent waves. It was found that acoustic evanescent waves can be resonantly amplified at the surface of a metamaterial slab with singly negative mass density [123,124], due to the interaction between the evanescent waves and the surface bound states. Subwavelength resolution was experimentally demonstrated in a membrane-type metamaterial with singly negative density [122].

Fabry–Pérot resonances produce flat dispersions over a wide range of wave vectors. Hence the wave vectors of the resonant modes can take very large values [125,126]. A holey structure with periodic subwavelength apertures (Fig. 6c) was designed and it was shown that the evanescent waves with large lateral wave vectors emanating from the source can be efficiently coupled to the Fabry–Pérot resonant modes and then be conveyed to the image plane in the vicinity of the structure [125]. These resonant modes carry the high spatial frequency information and contribute to the formation of a deep-subwavelength image with a linewidth of $\lambda/50$ at the image plane, far below the diffraction limit. Evanescent waves could also be converted to propagative waves by exciting trapped resonances inside acoustic waveguides [127]. Resolution ~5 times smaller than the operating wavelength was achieved and edge

detection was experimentally demonstrated using this type of metamaterial.

Resonance-based subwavelength imaging can only occur in a narrow frequency range. In order to achieve a broadband subwavelength imaging, non-resonant elements need to be utilized. Li *et al.* proposed a fin-shaped acoustic hyperlens (Fig. 6d) composed of alternating air and brass layers in the angular direction [128]. The term 'hyperlens' is related to its hyperbolic dispersion relation [129,130]. The dispersion relation for an acoustic wave in the polar coordinate system is given by $k_r{}^2/\rho_r + k_\theta{}^2/\rho_\theta = \omega^2/B$, with k_r and k_θ being the wave vectors along the radial and angular directions, respectively, and B being the bulk modulus. Here ρ_r and ρ_θ are the effective densities along the two directions. If ρ_r and ρ_θ take opposite signs, the dispersion relation satisfies a hyperbolic function for a given frequency and the wave vectors can take arbitrary values. In the fin-shaped structure, while the effective ρ_r and ρ_θ take the same sign, they differ greatly in magnitude. The dispersion relation is in the shape of an elongated ellipse and large wave vectors can be supported. By placing the sound source in the center of the lens, evanescent waves will be gradually converted to the propagation modes along the radial direction, and subwavelength features can be observed in the far field. This fin-shaped hyperlens is efficient for a wide frequency range due to its non-resonant characteristic. Besides these methods mentioned above, we note that the time-reversal technique has also been applied to obtain deep-subwavelength focal spots inside the acoustic resonator arrays [131].

Acoustic invisibility cloaking

Cloaking is an almost magical concept, often used in science fiction and movies, and possesses tremendous prospects for security and military applications. An object is invisible to incoming waves if it neither reflects nor absorbs. A feasible cloaking strategy is to guide the wave around the object so that the wavefront restores to its unscattered state after passing the object [132,133]. The mathematical technique, known as transformation optics, enables us to design a medium with a spatially varying refractive index to curve light around an object, which is based on the form invariance of Maxwell's equations, for electromagnetic waves, under coordinate transformations [134]. Transformation acoustics was proposed by mapping the acoustic equations to the single polarization Maxwell's equations in 2D space, or the electrical conductivity equation in both 2D and 3D space [45,135–138]. The time-harmonic acoustic equation can be expressed as

$$\nabla \cdot [\overleftrightarrow{\rho}(x)^{-1}\nabla p\,(x)] = -[\omega^2/\kappa\,(x)]p\,(x)\,, \tag{4}$$

where $\overleftrightarrow{\rho}(x)$ is the mass density tensor, $\kappa(x)$ is the bulk modulus, and $p(x)$ denotes the pressure field. After a coordinate transformation by mapping each point x to $x'(x)$ in the new space, the acoustic equation now becomes:

$$\begin{aligned}\nabla' \cdot [\overleftrightarrow{\rho'}(x')^{-1}\nabla' p'(x')] \\ = -[\omega^2/\kappa'(x')]p'(x'),\end{aligned} \tag{5}$$

The new equation maintains the same form while the parameters $\overleftrightarrow{\rho'}(x')^{-1}$ and $\kappa'(x')$ are related to the original $\overleftrightarrow{\rho}(x)^{-1}$ and $\kappa(x)$ by the Jacobian transformation matrix A: $\overleftrightarrow{\rho'}(x')^{-1} = A[\overleftrightarrow{\rho}(x)^{-1}]A^T/\det A$ and $\kappa'(x') = \det A \times \kappa(x)$, with $A_{ki} = \partial x'_k/\partial x_i$. This indicates that acoustic waves propagating in materials with complex parameters $\overleftrightarrow{\rho'}(x')$ and $\kappa'(x')$ will be guided as if they are passing through the transformed space. The equivalence between the material properties and coordinate transformations enables us to control acoustic waves in arbitrary ways and realize many intriguing effects, such as acoustic cloaking.

A 3D acoustic cloaking system can be designed by compressing the region $0 < r < b$ into the smaller region $a < r < b$, where a and b denote the inner and outer radii of the cloaking shell [137]. The cloaking shell will deflect the incident waves, and objects in the concealed region $0 < r < a$ become invisible. To realize the cloaking effect, the radial transformation is $r' = a + r(b-a)/b$, while the azimuthal angle φ and polar angle θ remain the same. The material parameters $\overleftrightarrow{\rho'}(x')$ and $\kappa'(x')$ in the cloaking shell can now be expressed as

$$\begin{aligned}\rho'_r &= \frac{b-a}{b}\frac{r'^2}{(r'-a)^2}\rho_0,\\ \rho'_\theta &= \rho'_\varphi = \frac{b-a}{b}\rho_0,\\ \kappa' &= \frac{(b-a)^3}{b^3}\frac{r'^2}{(r'-a)^2}\kappa_0.\end{aligned} \tag{6}$$

A feasible approach to realize the desired anisotropic mass density and isotropic modulus is by utilizing alternating isotropic layers consisting of solid cylinders embedded in the host fluid [139,140]. However, the mass density is seen to approach infinity near the inner boundary of the cloaking shell, which

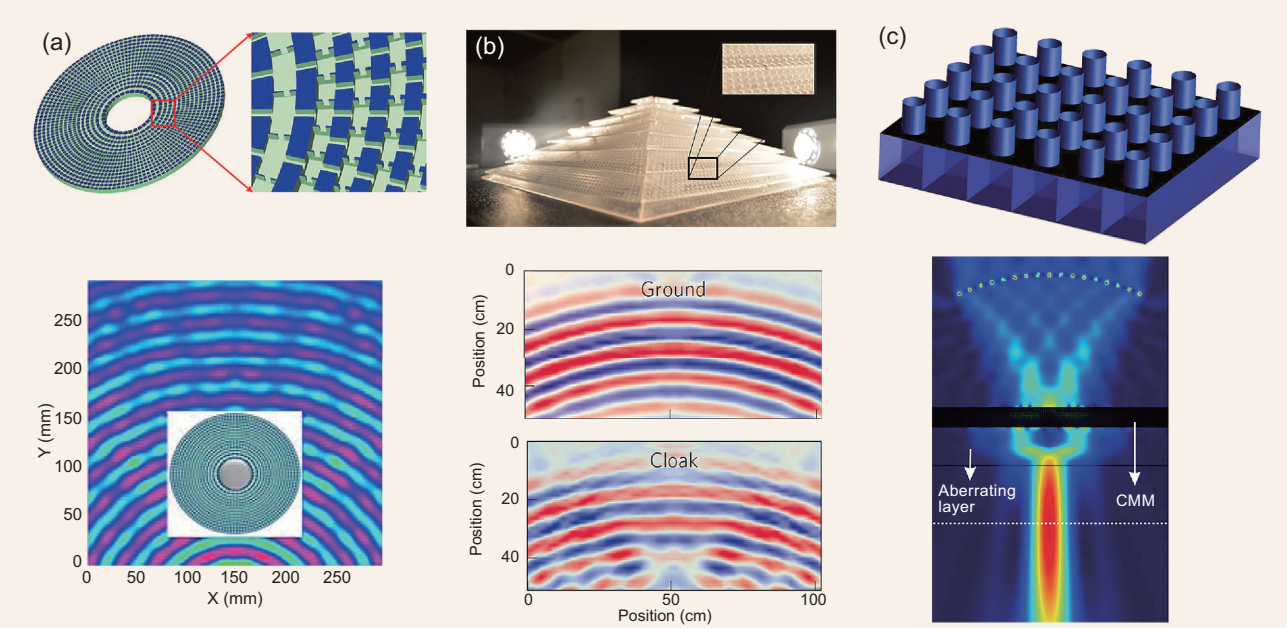

Figure 7. (a) A 2D cloak for underwater ultrasound waves. (b) A 3D carpet cloak for airborne sound. (c) The complementary material can acoustically cancel out the aberrating layers, such as the skull, in medical imaging applications. (a) adapted with permission from [147], Copyright 2011, American Physical Society; (b) adapted with permission from [150], Copyright 2014, Macmillan Publishers Ltd; (c) adapted from [154].

is difficult to truly realize. Norris demonstrated that acoustic cloaking can alternatively be achieved by using materials with anisotropic bulk modulus and isotropic mass density, known as pentamode materials [141,142]. Pentamode materials were first theoretically proposed by Milton *et al.* [143] and then realized by Kadic *et al.* through 3D laser lithography [144]. Pentamode materials are fluid-like solid materials with negligible shear modulus, and can provide highly anisotropic bulk modulus through interconnected microstructures [145,146].

Acoustic cloaking was first experimentally realized for underwater ultrasonic waves using a planar network of subwavelength cavities connected by narrow channels, and machined in the annular substrate as shown in Fig. 7a [147]. The geometric parameters of the cavities and channels were spatially tailored, based on the acoustic transmission line method. After putting the object inside the annular cloaking shell, the nearly undisturbed wavefront after passing through the object confirmed the cloaking effect. Another cloaking strategy, carpet cloaking [148], was later demonstrated for airborne sound in both 2D and 3D space [149,150]. The linear coordinate transformation in the carpet cloaking strategy results in homogeneous material parameters in the cloaking shell, which are easier to realize. The carpet cloaking hid the object under a pyramid-like shell made of perforated rigid plates and mimicked a flat reflecting surface (see Fig. 7b). The perforated plates here provided the desired anisotropic mass density. Recently, carpet cloaking for underwater acoustic waves was achieved by utilizing a structure with alternating brass and water layers in a deep-subwavelength scale [151]. In addition to acoustic cloaking, illusion acoustics was also proposed based on the transformation acoustics technique [152,153]. The illusion device conceals the original object and creates the image of another object instead. The illusion device, or complementary material specifically, can also open a virtual 'hole' in a rigid wall [152]. A type of complementary material with negative acoustic index was proposed (Fig. 7c) to cancel the aberrating intermediate layers between source and target and thereby allow high transmission of ultrasound in medical imaging applications [154]. The transformation acoustics technique has also been applied to the design of bifunctional lenses; for instance, in one direction one such device can operate as a fisheye lens for focusing a point source near the perimeter of the lens, and in the orthogonal direction, the device can operate as a Luneburg lens to collimate sound waves from a point-sized emitter [155].

Phase engineering and acoustic metasurfaces

Acoustic phased arrays can produce steerable and focused beams by dynamically modulating the phase delay in each independent transducer. By designing the phase distribution in the emitting plane, the phased array is capable of generating com-

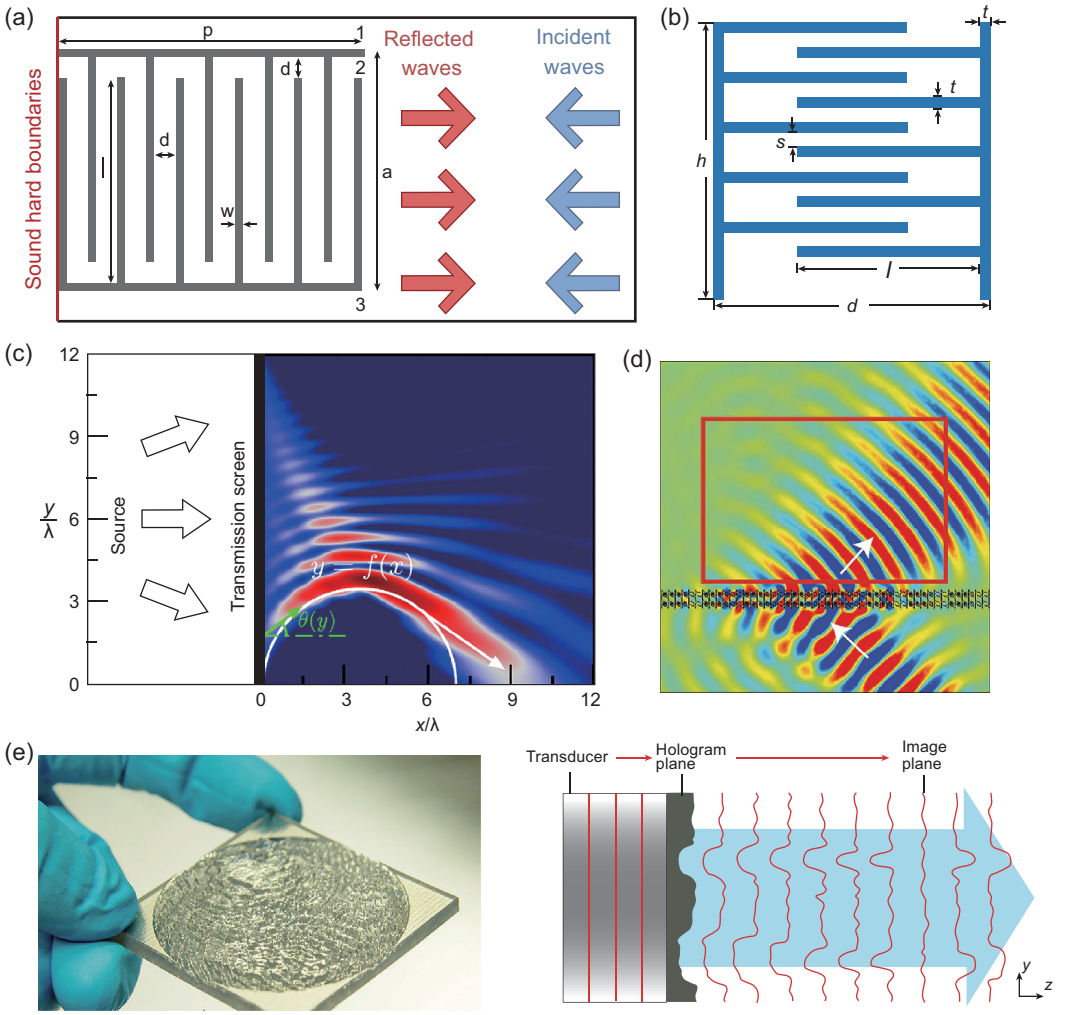

Figure 8. The coiled units enable substantial phase delays for the reflected waves (a) and transmitted waves (b). (c) The self-bending beam generated by the metasurface. (d) Negative refraction of the transmitted acoustic wave through the thin layer metasurface. (e) The hologram with a rough surface is fabricated by the 3D printer. The phase delay of each pixel is proportional to its thickness. (a) adapted with permission from [159], Copyright 2013, Macmillan Publishers Ltd; (b) adapted from [162]; (c) adapted with permission from [164], Copyright 2015, American Physical Society; (d) adapted with permission from [161], Copyright 2014, Macmillan Publishers Ltd; (e) adapted with permission from [171], Copyright 2016, Macmillan Publishers Ltd.

plex acoustic beams, such as acoustic vortex beams and self-bending beams with arbitrary trajectories [156,157]. Acoustic vortex beams with different 'topological charges' can be utilized as orthogonal channels to improve the data transmission rate for underwater acoustic communication [157]. In a recent work, an acoustic phased array was also employed to generate the desired field for trapping and translating levitated particles by optimizing the phase profile applied to the transducers [158]. However, the complex driving electronics and the large number of transducers can hamper its broad applications. In contrast to dynamically adaptable phased arrays, acoustic metasurfaces [159–169] are passive, planar structures with subwavelength thicknesses that can exhibit engineered phase distribution, with wavefront-shaping capabilities. Each unit cell on the metasurface is capable of generating a phase shift by utilizing coiled structures. The coiled structure forces acoustic waves to propagate along an internal zigzag path [68], shown in Fig. 8a, b, that provides substantial phase delays covering the whole range of 0 to 2π. Anomalous reflection and refraction behaviors have been demonstrated in metasurfaces by introducing a transversal phase gradient on the surface [160–162]. The refraction and reflection angles now obey the generalized Snell's law and take anomalous values due to the transversal momentum provided by the metasurface. Negative refraction (Fig. 8d) and conversion from propagating mode to surface mode were both experimentally verified. Like phased arrays, metasurfaces can be used to gen-

erate self-bending beams (Fig. 8c) and vortex beams via designed in-plane phase profiles [164,166,167]. Unlike the coiled structure, a hybrid structure comprising Helmholtz cavities and a straight channel was recently proposed to realize the target phase delay [166]. Here the straight-channel Fabry–Pérot resonator serves the purpose of impedance matching to the incident wave, while the Helmholtz resonators modulate the effective wave vectors. However, the thickness of such a hybrid structure can reach half-wavelength, much larger than the coiled structures. Besides the intriguing phase engineering capability, acoustic metasurfaces can also realize asymmetric transmission by utilizing lossy acoustic metasurfaces [170]. Due to the lack of sufficient impedance contrast between water and solid materials, acoustic metasurfaces for underwater applications have yet to be extensively studied.

A simple strategy to realize acoustic holography was recently reported [171]. The monolithic acoustic hologram was fabricated by 3D printing and the phase delay of each pixel in the hologram is proportional to its thickness (see Fig. 8e). The hologram was placed in front of a planar transducer to modify the wavefront of the transmitted ultrasound in water. A complex image with diffraction-limited resolution was formed in the image plane by encoding the required phase profile in the hologram. The hologram is also capable of manipulating particles in various ways by freely designing the amplitude and phase distributions in the reconstructed acoustic field. Compared with the commercial phased array, this technique is simple and inexpensive, and provides much higher degrees of freedom for reconstructing acoustic fields. An acoustic hologram based on coiled structures was demonstrated in yet another recent paper [172].

Sound absorption

The high energy density concentrated by the local resonance of metamaterials is favorable for sound absorption since the energy dissipation power is the product of the local energy density and the dissipative coefficient [173]. One example is DMRs, which are capable of highly concentrating the sound energy at the edges of the decorated rigid platelets, as shown in Fig. 9a [174]. By means of the intrinsic viscosity of membrane, the incoming sound energy can be efficiently dissipated within the thickness of the membranes, ∼1/10 000 of the relevant wavelengths. However, such absorption by thin film has an intrinsic 50% limit due to the geometric constraint [173,175]. As the relative motion between the two surfaces of the membrane was frozen at low frequencies, the relevant vibration modes are all dipolar in character, and can only couple to the antisymmetric components from the environmental fields. Since the sound incident from one side can be decomposed into two equally weighted symmetric (monopolar) and antisymmetric (dipolar) components, only half of the energy can couple to the motions of the membranes and the maximum absorption can only reach 50%. This upper bound in absorption has been theoretically and experimentally demonstrated by Yang *et al.* [175]. Similar limits also exist for symmetric resonators. For example, Merkel *et al.* showed that an HR on the sidewall of a duct can only absorb the energy of one-way traveling sounds in the duct maximally by 50% [176]. Leroy *et al.* found a similar limit for waterborne sounds absorbed by bubbles in a solid soft medium [177]. To overcome such limits, the coherent perfect absorption (CPA) approach has been proposed [178]. By introducing a control sound wave incident from the opposite direction, the resulting sound field can be purely symmetric (antisymmetric) if the control waves are in (out of) phase and have the intensity equal to the original sounds. Therefore, all the energy from both the original and control waves can couple to the absorber and be completely dissipated if the critical coupling condition is satisfied [179]. Such acoustic CPA has been theoretically predicted and numerically demonstrated by Wei *et al.* [180] and Yang *et al.* [181] and experimentally realized by Meng *et al.* [182]. Song *et al.* extended the acoustic CPA concept into the 2D scenario with higher-order symmetries such as quadrupole and octupole resonances [183]. An alternative way to attain 100% absorption is using a pair of degenerate resonators (Fig. 9b) that have two different symmetries in the same frequency [184]. In this context, no matter what ambient sound field is applied, the energy can always be fully coupled to the absorber and hence totally dissipated.

The aforementioned limit applies only to the absorption occurring during a single scattering event. One can expect to break such a limit by introducing multiple scatterings [173,175]. By placing a rigid wall behind the DMR (see Fig. 9c), multiple reflections between the wall and the DMR can bring the absorption of a sound wave incident from one side to near unity. Ma *et al.* demonstrated that greater than 99% of the incoming energy can be absorbed with a thin air gap between the DMR and the reflecting wall that is smaller than 1/100 of the relevant wavelength [163]. A similar mechanism works for HR as well. Romero-García *et al.* demonstrated such total absorption by one HR on the sidewall of a duct with the dead end being the reflective wall and broadband absorption comprising four peaks from four dif-

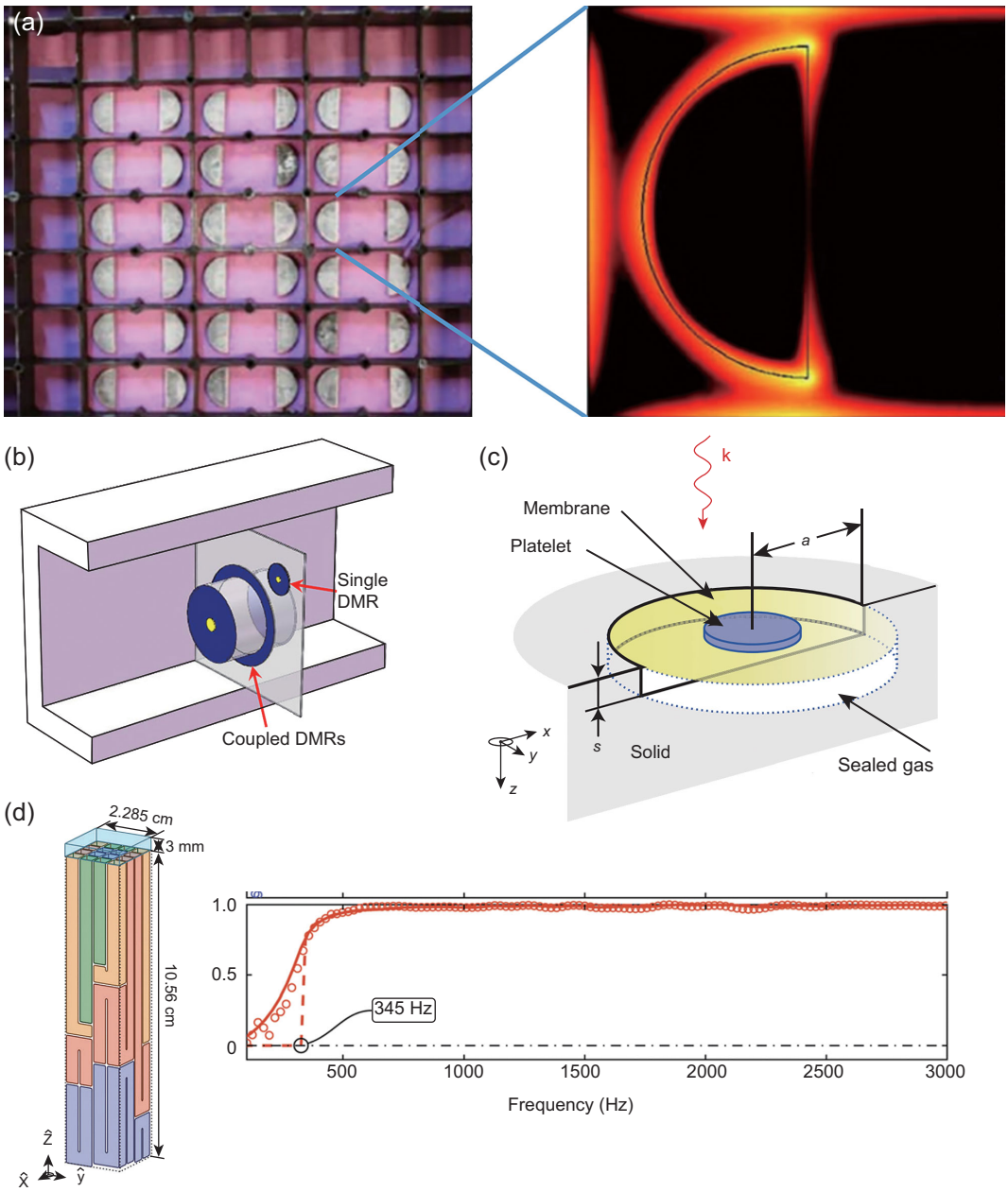

Figure 9. (a) The DMRs can highly concentrate the sound energy at the edges of the decorated rigid platelets. (b), (c) Total absorption for one-side incoming waves can be achieved by utilizing a pair of degenerate resonators (b) or introducing multiple reflections (c). (d) The optimal absorber exhibits a very flat absorption spectrum in a semi-infinite frequency range. (a) adapted with permission from [174], Copyright 2012, Macmillan Publishers Ltd; (b) adapted with permission from [184], Copyright 2015, AIP Publishing; (c) adapted with permission from [163], Copyright 2014, Macmillan Publishers Ltd; (d) adapted with permission from [194], Copyright 2017, Royal Society of Chemistry.

ferent HRs [185]. By using similar HR structures, Jimenez *et al.* reported quasi-omnidirectional and total absorption of sound by a composite panel [186]. The conventional porous materials can also be improved by introducing resonances and achieve total absorption with rigid backing [187–192]. In other works, Merkel *et al.* [176] and Fu *et al.* [193] showed that two different resonators, aligned in sequence, can exhibit total absorption of sound; in this arrangement the back resonator's anti-resonance played the role of a reflective wall.

Due to the resonant feature, subwavelength metamaterial absorbers are usually narrowband in character. For example, in Ref. [163], the full width at half maximum of the absorption peak is only about 1/127 of the central frequency. This has recently been understood through the causality constraint in the sound absorption process: measuring the sound

pressure level dropping during scatterings on an absorber by decibels (dB), its integral over all the wavelengths has an upper limit that is proportional to the absorber's thickness [173,194]:

$$d \geq \frac{1}{4\pi^2}\frac{B_{\text{eff}}}{B_0}\left|\int_0^{\infty} \ln\left[1 - A\left(\lambda\right)\right] d\lambda\right|. \qquad (7)$$

Here d is the thickness of an absorber, B_{eff} is its effective bulk modulus at the static limit, B_0 denotes the air bulk modulus, and $A(\lambda)$ denotes the energy absorption spectrum. From equation (7), it is clear that the absorbers with a small d, i.e., very subwavelength thicknesses, can afford a high absorption $(A \to 1)$ only over a very narrow bandwidth.

A natural way to extend the absorption bandwidth is to stack multiple resonances with frequencies slightly differing from each other. Many attempts have been made along this direction [195–197]; however, the lack of a central integration principle results in only limited success. Recently, work on the causally optimal broadband absorber (COBA) has solved the problem by integrating the causal constraint, equation (7), into the absorbers' design strategy [194]. A causally optimal absorber is the one that can take the equals sign in equation (7). This means that the possible potential allowed by the absorbers' thickness d has been fully utilized, and the thickness of such an absorber is a priori knowledge for a target absorption spectrum $A(\lambda)$. For the spectrum approaching 1 over a broadband, one should only ensure that an absorber has the minimum thickness and the resonant modes distributed in the frequency range by a density that is inversely proportional to the relevant oscillator strengths. Therefore, based on an array of folded Fabry–Pérot tubes, a very flat absorption spectrum approaching unity has been realized in a semi-infinite frequency range starting from a lower cutoff that corresponds to a wavelength about nine times larger than the absorber thickness (Fig. 9d).

PT-symmetry synthetic acoustics

The inevitable presence of dissipation in acoustic metamaterials can limit the efficiency of the devices. It is therefore desirable to minimize the inherent losses, which is sometimes difficult to realize. An alternative approach is to introduce active components as a gain medium, to compensate the losses. The balanced loss–gain system not only supports lossless wave transmission, but also introduces a variety of intriguing phenomena in wave manipulation that may be regarded as the result of tuning the imaginary part of the refractive index. Such a balanced loss–gain system is related to the parity–time (PT) symmetry of the Hamiltonian that describes the system, which was first investigated in the quantum mechanics of lossy systems. The concept was subsequently explored in the realm of classical waves. In quantum mechanics, it is stated that the Hamiltonian needs to be Hermitian in order to ensure a real eigenvalue spectrum. However, Bender and Boettcher in their seminal work demonstrated that even a non-Hermitian system can exhibit real energy eigenspectra if the non-Hermitian Hamiltonian possesses PT symmetry [198]. A system is PT symmetric if it is invariant under combined parity operation $\hat{p} \to -\hat{p}, \hat{x} \to -\hat{x}$ and time-reversal operation $\hat{p} \to -\hat{p}, \hat{x} \to \hat{x}, i \to -i$. An important characteristic of PT-symmetric systems is the existence of spontaneous PT-symmetry breaking at the exceptional point, where the real eigenvalues coalesce and form complex conjugate pairs beyond the exceptional point. For optical and acoustic systems, if the refractive index satisfies the relation $n(x) = n^*(-x)$, which corresponds to a balanced distribution of gain and loss, then these systems are PT symmetric and the eigenstates can have real eigenvalues. Engineering the imaginary part of the refractive index provides us with more degrees of freedom to control optical and acoustic waves. The field of PT photonics has drawn considerable attention and numerous intriguing phenomena have been demonstrated, such as unidirectional transparency [199], coherent perfect absorber (CPA) lasers [200], nonreciprocal propagation [201], and single-mode lasing [202].

In order to construct PT-symmetric acoustic systems, it is crucial to introduce the gain and loss elements for acoustic waves [46]. Several feasible designs have been proposed. For airborne sound, loudspeakers loaded with electronic circuits can be utilized as tunable unit cells to meet the desired loss and gain conditions by actively absorbing or injecting energy [47,203,204]. Elastic waves propagating in a piezoelectric semiconductor slab can be amplified or attenuated by controlling the electric bias. By delicately stacking slabs biased in different directions, the PT-symmetric condition can be realized in theory [205]. However, experimental realization has yet to be achieved. For acoustic waves in a flow duct, it is interesting to find out that the vortex–sound interaction at discontinuous boundaries can give rise to the flow-induced effective gain and loss [206]. These PT-symmetric acoustic systems mentioned above are all 1D systems comprising a pair of loss and gain units, and researchers mainly focus on the scattering behaviors of acoustic waves, such as unidirectional transparency at the exceptional point. Higher

dimensional or periodic systems and the intriguing phenomena related to the PT broken phase remain to be explored. Recently, the emergence and coalescence of exceptional points in coupled acoustic lossy cavities has been studied [207]. By introducing asymmetric losses in cavities, the system demonstrated similar characteristics to the PT-symmetric systems.

CONCLUSIONS AND OUTLOOK

In this article, we have focused on reviewing the developments in the field of acoustic waves. Even though elastic and mechanical metamaterials have also been extensively studied in recent years [208–210], a survey of such works is beyond the chosen scope of this review. To conclude, we would like to note that there remain some challenges to overcome before real-world applications of recently developed phenomena can be realized. In particular, the resonance-induced narrow working bandwidth and inherent losses are limiting factors for the applications of acoustic metamaterials. One possible solution could be the designed integration of resonances as in the realization of the broadband acoustic absorber [194]. Another possible solution is to utilize tunable active metamaterials [211,212]. Another challenge lies in water acoustics. The low impedance contrast between water and solid materials requires new design schemes for underwater applications.

In the view of the fundamental sciences, the unusual properties of acoustic metamaterials can be predicted by the effective medium theory. What is the ultimate limit of the effective medium theory at very low frequencies? Nonlinear acoustics is an important branch of acoustics and we may raise the question about what are the avenues to harness the nonlinear effects in phononic crystals and acoustic metamaterials. For example, how can acoustic waves be used to manipulate condensed matter, such as photons [213] and electrons in the near field, or vice versa? Also, we envision that with advanced micro/nanofabrication, the operation frequency of phononic crystals could be extended to higher-frequency regimes (hundreds of MHz to a few THz?), so manipulation of heat flow can be possible [24,214].

We have seen that quantum phenomena in condensed matter can also be explored in classical acoustic systems. Below we speculate on the future. Can the concept of metamaterials and phononic crystals be evolved into quantum systems? For example, can high-frequency acoustic waves, i.e., phonons, be made to couple to superconducting circuits and qubits [215]? What are possible device architectures to measure the properties of single or small numbers of phonons (THz and below)? The discovery of such devices would enable precision metrology of acoustics in the quantum domain. As the quantum–classical analogies have motivated the development of phononic crystals and acoustic metamaterials, the areas of topological acoustics and PT-symmetric acoustics, which also owe their beginnings to quantum mechanics, are now growing rapidly with promising potential applications. Topological acoustics have demonstrated one-way propagation edge modes. Can these effects be turned into useful one-way waveguides, delay lines, wave splitters with high signal–noise ratio, and resonators with high Q factors [216]? In addition, how can the acoustic gain and experimental implantation in PT-symmetric elastic systems [205] be obtained? The above are just a few challenges facing the acoustics community. We believe that resolution of any one of these challenges could lead to a breakthrough in applications.

Hopefully, this review has given readers a snapshot of the very rapidly evolving field of phononic crystals and acoustic metamaterials. If there is a perceptible trend, it is that the field is becoming broader and deeper, with no end in sight.

FUNDING

This work was supported by the National Key R&D Program of China (2017YFA0303702, 2017YFA0305100), and the National Natural Science Foundation of China (11625418, 11474158, 51732006, 51721001, and 51472114). We also acknowledge the support of the Natural Science Foundation of Jiangsu Province (BK20140019). Dr Min Yang and Prof. Ping Sheng acknowledge the support of Hong Kong Government grants (AoE/P-02/12 and ITF UIM29). Dr Chu Ma and Prof. Nicholas Fang acknowledge the support from the Multidisciplinary University Research Initiative from the Office of Naval Research (N00014–13-1–0631).

REFERENCES

1. Yablonovitch E. Inhibited spontaneous emission in solid-state physics and electronics. *Phys Rev Lett* 1987; **58**: 2059–62.
2. John S. Strong localization of photons in certain disordered dielectric superlattices. *Phys Rev Lett* 1987; **58**: 2486–9.
3. Sigalas M and Economou EN. Band structure of elastic waves in two dimensional systems. *Solid State Commun* 1993; **86**: 141–3.
4. Kushwaha MS, Halevi P and Dobrzynski L *et al.* Acoustic band structure of periodic elastic composites. *Phys Rev Lett* 1993; **71**: 2022–5.

5. Pennec Y, Vasseur JO and Djafari-Rouhani B *et al.* Two-dimensional phononic crystals: examples and applications. *Surf Sci Rep* 2010; **65**: 229–91.
6. Deymier PA. *Acoustic Metamaterials and Phononic Crystals*. Berlin: Springer, 2013.
7. Hussein MI, Leamy MJ and Ruzzene M. Dynamics of phononic materials and structures: historical origins, recent progress, and future outlook. *Appl Mech Rev* 2014; **66**: 040802–38.
8. Laude V. *Phononic Crystals: Artificial Crystals for Sonic, Acoustic and Elastic Waves*. Berlin: De Gruyter, 2015.
9. Khelif A and Adibi A. *Phononic Crystals: Fundamentals and Applications*. New York: Springer, 2016.
10. Martínez-Sala R, Sancho J and Sánchez JV *et al.* Sound attenuation by sculpture. *Nature* 1995; **378**: 241.
11. Sánchez-Pérez JV, Caballero D and Mártinez-Sala R *et al.* Sound attenuation by a two-dimensional array of rigid cylinders. *Phys Rev Lett* 1998; **80**: 5325–8.
12. Christensen J, Fernandez-Dominguez AI and de Leon-Perez F *et al.* Collimation of sound assisted by acoustic surface waves. *Nat Phys* 2007; **3**: 851–2.
13. Christensen J, Martin-Moreno L and Garcia-Vidal FJ. Theory of resonant acoustic transmission through subwavelength apertures. *Phys Rev Lett* 2008; **101**: 014301.
14. Lu MH, Liu XK and Feng L *et al.* Extraordinary acoustic transmission through a 1D grating with very narrow apertures. *Phys Rev Lett* 2007; **99**: 174301.
15. Zhang XD and Liu ZY. Extremal transmission and beating effect of acoustic waves in two-dimensional sonic crystals. *Phys Rev Lett* 2008; **101**: 264303.
16. Torrent D and Sánchez-Dehesa J. Acoustic analogue of graphene: observation of Dirac cones in acoustic surface waves. *Phys Rev Lett* 2012; **108**: 174301.
17. Yu SY, Sun XC and Ni X *et al.* Surface phononic graphene. *Nat Mater* 2016; **15**: 1243–7.
18. Hasan MZ and Kane CL. Colloquium: topological insulators. *Rev Mod Phys* 2010; **82**: 3045–67.
19. Qi XL and Zhang SC. Topological insulators and superconductors. *Rev Mod Phys* 2011; **83**: 1057–110.
20. Lu L, Joannopoulos JD and Soljačić M. Topological photonics. *Nat Photon* 2014; **8**: 821–9.
21. Sun XC, He C and Liu XP *et al.* Two-dimensional topological photonic systems. *Progr Quant Electron* 2017; **55**: 52–73.
22. Zhang LF, Ren J and Wang JS *et al.* Topological nature of the phonon Hall effect. *Phys Rev Lett* 2010; **105**: 225901.
23. Zhang LF, Ren J and Wang JS *et al.* The phonon Hall effect: theory and application. *J Phys: Condens Matter* 2011; **23**: 305402.
24. Li NB, Ren J and Wang L *et al. Colloquium*: Phononics: manipulating heat flow with electronic analogs and beyond. *Rev Mod Phys* 2012; **84**: 1045–66.
25. Yang ZJ, Gao F and Shi XH *et al.* Topological acoustics. *Phys Rev Lett* 2015; **114**: 114301.
26. Xiao M, Ma GC and Yang ZY *et al.* Geometric phase and band inversion in periodic acoustic systems. *Nat Phys* 2015; **11**: 240–4.
27. Xiao M, Chen WJ and He WY *et al.* Synthetic gauge flux and Weyl points in acoustic systems. *Nat Phys* 2015; **11**: 920–4.
28. He C, Ni X and Ge H *et al.* Acoustic topological insulator and robust one-way sound transport. *Nat Phys* 2016; **12**: 1124–9.
29. Liu ZY, Zhang XX and Mao YW *et al.* Locally resonant sonic materials. *Science* 2000; **289**: 1734–6.
30. Milton GW and Willis JR. On modifications of Newton's second law and linear continuum elastodynamics. *Proc R Soc Lond A* 2007; **463**: 855–80.
31. Liu ZY, Chan CT and Sheng P. Analytic model of phononic crystals with local resonances. *Phys Rev B* 2005; **71**: 014103.
32. Cummer SA, Christensen J and Alù A. Controlling sound with acoustic metamaterials. *Nat Rev Mater* 2016; **1**: 16001.
33. Ma GC and Sheng P. Acoustic metamaterials: from local resonances to broad horizons. *Sci Adv* 2016; **2**: e1501595.
34. Wong ZJ, Wang Y and Kevin OB *et al.* Optical and acoustic metamaterials: superlens, negative refractive index and invisibility cloak. *J Opt* 2017; **19**: 084007.
35. Lu MH, Feng L and Chen YF. Phononic crystals and acoustic metamaterials. *Mater Today* 2009; **12**: 34–42.
36. Li J and Chan CT. Double-negative acoustic metamaterial. *Phys Rev E* 2004; **70**: 055602.
37. Fang N, Xi DJ and Xu JY *et al.* Ultrasonic metamaterials with negative modulus. *Nat Mater* 2006; **5**: 452–6.
38. Wu Y, Lai Y and Zhang ZQ. Effective medium theory for elastic metamaterials in two dimensions. *Phys Rev B* 2007; **76**: 205313.
39. Mei J, Liu ZY and Wen WJ *et al.* Effective dynamic mass density of composites. *Phys Rev B* 2007; **76**: 134205.
40. Fokin V, Ambati M and Sun C *et al.* Method for retrieving effective properties of locally resonant acoustic metamaterials. *Phys Rev B* 2007; **76**: 144302.
41. Zigoneanu L, Popa B-I and Starr AF *et al.* Design and measurements of a broadband two-dimensional acoustic metamaterial with anisotropic effective mass density. *J Appl Phys* 2011; **109**: 054906.
42. Yang M, Ma GC and Wu Y *et al.* Homogenization scheme for acoustic metamaterials. *Phys Rev B* 2014; **89**: 064309.
43. Lee SH, Park CM and Seo YM *et al.* Reversed Doppler effect in double negative metamaterials. *Phys Rev B* 2010; **81**: 241102.
44. Kaina N, Lemoult F and Fink M *et al.* Negative refractive index and acoustic superlens from multiple scattering in single negative metamaterials. *Nature* 2015; **525**: 77–81.
45. Chen HY and Chan CT. Acoustic cloaking and transformation acoustics. *J Phys D: Appl Phys* 2010; **43**: 113001.
46. Zhu XF, Ramezani H and Shi CZ *et al.* PT-symmetric acoustics. *Phys Rev X* 2014; **4**: 031042.
47. Fleury R, Sounas D and Alù A. An invisible acoustic sensor based on parity-time symmetry. *Nat Commun* 2015; **6**: 5905.
48. Veselago VG. The electrodynamics of substances with simultaneously negative values of ϵ and μ. *Sov Phys Usp* 1968; **10**: 509–14.
49. Zhang XD and Liu ZY. Negative refraction of acoustic waves in two-dimensional phononic crystals. *Appl Phys Lett* 2004; **85**: 341–3.
50. Feng L, Liu XP and Chen YB *et al.* Negative refraction of acoustic waves in two-dimensional sonic crystals. *Phys Rev B* 2005; **72**: 033108.
51. Feng L, Liu XP and Lu MH *et al.* Acoustic backward-wave negative refractions in the second band of a sonic crystal. *Phys Rev Lett* 2006; **96**: 014301.
52. Yang SX, Page JH and Liu ZY *et al.* Focusing of sound in a 3D phononic crystal. *Phys Rev Lett* 2004; **93**: 024301.
53. Ke MZ, Liu ZY and Qiu C *et al.* Negative-refraction imaging with two-dimensional phononic crystals. *Phys Rev B* 2005; **72**: 064306.
54. Qiu CY, Zhang XD and Liu ZY. Far-field imaging of acoustic waves by a two-dimensional sonic crystal. *Phys Rev B* 2005; **71**: 054302.
55. Sukhovich A, Merheb B and Muralidharan K *et al.* Experimental and theoretical evidence for subwavelength imaging in phononic crystals. *Phys Rev Lett* 2009; **102**: 154301.
56. Lu MH, Zhang C and Feng L *et al.* Negative birefraction of acoustic waves in a sonic crystal. *Nat Mater* 2007; **6**: 744–8.
57. Gerritsma R, Kirchmair G and Zähringer F *et al.* Quantum simulation of the Dirac equation. *Nature* 2010; **463**: 68–71.

58. Novoselov KS, Geim AK and Morozov SV *et al.* Two-dimensional gas of massless Dirac fermions in graphene. *Nature* 2005; **438**: 197–200.
59. Wilson M. Electrons in atomically thin carbon sheets behave like massless particles. *Phys Today* 2006; **59**: 21–3.
60. Novoselov KS, Fal'ko VI and Colombo L *et al.* A roadmap for graphene. *Nature* 2012; **490**: 192–200.
61. Ochiai T and Onoda M. Photonic analog of graphene model and its extension: Dirac cone, symmetry, and edge states. *Phys Rev B* 2009; **80**: 155103.
62. Mei J, Wu Y and Chan CT *et al.* First-principles study of Dirac and Dirac-like cones in phononic and photonic crystals. *Phys Rev B* 2012; **86**: 035141.
63. Lu JY, Qiu CY and Xu SJ *et al.* Dirac cones in two-dimensional artificial crystals for classical waves. *Phys Rev B* 2014; **89**: 134302.
64. Zhang XD. Observing Zitterbewegung for photons near the Dirac point of a two-dimensional photonic crystal. *Phys Rev Lett* 2008; **100**: 113903.
65. Yang ZJ, Gao F and Yang YH *et al.* Strain-induced gauge field and Landau levels in acoustic structures. *Phys Rev Lett* 2017; **118**: 194301.
66. Silveirinha M and Engheta N. Tunneling of electromagnetic energy through subwavelength channels and bends using epsilon-near-zero materials. *Phys Rev Lett* 2006; **97**: 157403.
67. Edwards B, Alù A and Young ME *et al.* Experimental verification of epsilon-near-zero metamaterial coupling and energy squeezing using a microwave waveguide. *Phys Rev Lett* 2008; **100**: 033903.
68. Liang ZX and Li J. Extreme acoustic metamaterial by coiling up space. *Phys Rev Lett* 2012; **108**: 114301.
69. Fleury R and Alù A. Extraordinary sound transmission through density-near-zero ultranarrow channels. *Phys Rev Lett* 2013; **111**: 055501.
70. Graciá-Salgado R, García-Chocano VM and Torrent D *et al.* Negative mass density and ρ-near-zero quasi-two-dimensional metamaterials: design and applications. *Phys Rev B* 2013; **88**: 224305.
71. Zheng LY, Wu Y and Ni X *et al.* Acoustic cloaking by a near-zero-index phononic crystal. *Appl Phys Lett* 2014; **104**: 161904.
72. Huang XQ, Lai Y and Hang ZH *et al.* Dirac cones induced by accidental degeneracy in photonic crystals and zero-refractive-index materials. *Nat Mater* 2011; **10**: 582–6.
73. Liu FM, Huang XQ and Chan CT. Dirac cones at $k\rightarrow = 0$ in acoustic crystals and zero refractive index acoustic materials. *Appl Phys Lett* 2012; **100**: 071911.
74. Dubois M, Shi CZ and Zhu XF *et al.* Observation of acoustic Dirac-like cone and double zero refractive index. *Nat Commun* 2017; **8**: 14871.
75. Shen SQ. The family of topological phases in condensed matter. *Natl Sci Rev* 2014; **1**: 49–59.
76. Klitzing KV, Dorda G and Pepper M. New method for high-accuracy determination of the fine-structure constant based on quantized Hall resistance. *Phys Rev Lett* 1980; **45**: 494–7.
77. Thouless DJ, Kohmoto M and Nightingale MP *et al.* Quantized Hall conductance in a two-dimensional periodic potential. *Phys Rev Lett* 1982; **49**: 405–8.
78. Haldane FDM and Raghu S. Possible realization of directional optical waveguides in photonic crystals with broken time-reversal symmetry. *Phys Rev Lett* 2008; **100**: 013904.
79. Wang Z, Chong YD and Joannopoulos JD *et al.* Observation of unidirectional backscattering-immune topological electromagnetic states. *Nature* 2009; **461**: 772–5.
80. Liang B, Guo XS and Tu J *et al.* An acoustic rectifier. *Nat Mater* 2010; **9**: 989–92.
81. Fleury R, Sounas DL and Sieck CF *et al.* Sound isolation and giant linear nonreciprocity in a compact acoustic circulator. *Science* 2014; **343**: 516–9.
82. Ni X, He C and Sun XC *et al.* Topologically protected one-way edge mode in networks of acoustic resonators with circulating air flow. *New J Phys* 2015; **17**: 053016.
83. Khanikaev AB, Fleury R and Mousavi SH *et al.* Topologically robust sound propagation in an angular-momentum-biased graphene-like resonator lattice. *Nat Commun* 2015; **6**: 8260.
84. Chen ZG and Wu Y. Tunable topological phononic crystals. *Phys Rev Appl* 2016; **5**: 054021.
85. Wang Q, Yang Y and Ni X *et al.* Acoustic asymmetric transmission based on time-dependent dynamical scattering. *Sci Rep* 2015; **5**: 10880.
86. Fang KJ, Yu ZF and Fan SH. Realizing effective magnetic field for photons by controlling the phase of dynamic modulation. *Nat Photon* 2012; **6**: 782–7.
87. Fleury R, Khanikaev AB and Alù A. Floquet topological insulators for sound. *Nat Commun* 2016; **7**: 11744.
88. He C, Sun XC and Liu XP *et al.* Photonic topological insulator with broken time-reversal symmetry. *Proc Natl Acad Sci USA* 2016; **113**: 4924–8.
89. Khanikaev AB, Hossein Mousavi S and Tse W-K *et al.* Photonic topological insulators. *Nat Mater* 2012; **12**: 233–9.
90. Wu LH and Hu X. Scheme for achieving a topological photonic crystal by using dielectric material. *Phys Rev Lett* 2015; **114**: 223901.
91. Mei J, Chen ZG and Wu Y. Pseudo-time-reversal symmetry and topological edge states in two-dimensional acoustic crystals. *Sci Rep* 2016; **6**: 32752.
92. Zhang ZW, Wei Q and Cheng Y *et al.* Topological creation of acoustic pseudospin multipoles in a flow-free symmetry-broken metamaterial lattice. *Phys Rev Lett* 2017; **118**: 084303.
93. Simon Y, Romain F and Fabrice L *et al.* Topological acoustic polaritons: robust sound manipulation at the subwavelength scale. *New J Phys* 2017; **19**: 075003.
94. Deng Y, Ge H and Tian Y *et al.* Observation of zone folding induced acoustic topological insulators and the role of spin-mixing defects. *Phys Rev B* 2017; **96**: 184305.
95. Chen ZG, Ni X and Wu Y *et al.* Accidental degeneracy of double Dirac cones in a phononic crystal. *Sci Rep* 2015; **4**: 4613.
96. Li Y, Wu Y and Mei J. Double Dirac cones in phononic crystals. *Appl Phys Lett* 2014; **105**: 014107.
97. Peng YG, Qin CZ and Zhao DG *et al.* Experimental demonstration of anomalous Floquet topological insulator for sound. *Nat Commun* 2016; **7**: 13368.
98. He C, Li Z and Ni X *et al.* Topological phononic states of underwater sound based on coupled ring resonators. *Appl Phys Lett* 2016; **108**: 031904.
99. Wei Q, Tian Y and Zuo SY *et al.* Experimental demonstration of topologically protected efficient sound propagation in an acoustic waveguide network. *Phys Rev B* 2017; **95**: 094305.
100. Lu JY, Qiu CY and Ye LP *et al.* Observation of topological valley transport of sound in sonic crystals. *Nat Phys* 2016; **13**: 369–74.
101. Vila J, Pal RK and Ruzzene M. Observation of topological valley modes in an elastic hexagonal lattice. *Phys Rev B* 2017; **96**: 134307.
102. Lu L, Wang ZY and Ye DX *et al.* Experimental observation of Weyl points. *Science* 2015; **349**: 622–4.
103. Li F, Huang X and Lu J *et al.* Weyl points and Fermi arcs in a chiral phononic crystal. *Nat Phys* 2018; **14**: 30–4.
104. Yang ZJ and Zhang BL. Acoustic type-II Weyl nodes from stacking dimerized chains. *Phys Rev Lett* 2016; **117**: 224301.
105. Lu L, Fang C and Fu L *et al.* Symmetry-protected topological photonic crystal in three dimensions. *Nat Phys* 2016; **12**: 337–40.

106. Zeuner JM, Rechtsman MC and Plotnik Y *et al.* Observation of a topological transition in the bulk of a non-Hermitian system. *Phys Rev Lett* 2015; **115**: 040402.
107. Leykam D, Bliokh KY and Huang C *et al.* Edge modes, degeneracies, and topological numbers in non-Hermitian systems. *Phys Rev Lett* 2017; **118**: 040401.
108. Yang Z, Mei J and Yang M *et al.* Membrane-type acoustic metamaterial with negative dynamic mass. *Phys Rev Lett* 2008; **101**: 204301.
109. Lee SH, Park CM and Seo YM *et al.* Acoustic metamaterial with negative density. *Phys Lett A* 2009; **373**: 4464–9.
110. Sui N, Yan X and Huang T-Y *et al.* A lightweight yet sound-proof honeycomb acoustic metamaterial. *Appl Phys Lett* 2015; **106**: 171905.
111. Lee SH, Park CM and Seo YM *et al.* Acoustic metamaterial with negative modulus. *J Phys: Condens Matter* 2009; **21**: 175704.
112. Ding YQ, Liu ZY and Qiu CY *et al.* Metamaterial with simultaneously negative bulk modulus and mass density. *Phys Rev Lett* 2007; **99**: 093904.
113. Lee SH, Park CM and Seo YM *et al.* Composite acoustic medium with simultaneously negative density and modulus. *Phys Rev Lett* 2010; **104**: 054301.
114. Fok L and Zhang X. Negative acoustic index metamaterial. *Phys Rev B* 2011; **83**: 214304.
115. Yang M, Ma GC and Yang ZY *et al.* Coupled membranes with doubly negative mass density and bulk modulus. *Phys Rev Lett* 2013; **110**: 134301.
116. Brunet T, Merlin A and Mascaro B *et al.* Soft 3D acoustic metamaterial with negative index. *Nat Mater* 2014; **14**: 384–8.
117. Xie YB, Popa B-I and Zigoneanu L *et al.* Measurement of a broadband negative index with space-coiling acoustic metamaterials. *Phys Rev Lett* 2013; **110**: 175501.
118. Pendry JB. Negative refraction makes a perfect lens. *Phys Rev Lett* 2000; **85**: 3966–9.
119. Fang N, Lee H and Sun C *et al.* Sub-diffraction-limited optical imaging with a silver superlens. *Science* 2005; **308**: 534–7.
120. Zhang X and Liu ZW. Superlenses to overcome the diffraction limit. *Nat Mater* 2008; **7**: 435–41.
121. Zhang S, Yin LL and Fang N. Focusing ultrasound with an acoustic metamaterial network. *Phys Rev Lett* 2009; **102**: 194301.
122. Park JJ, Park CM and Lee KJB *et al.* Acoustic superlens using membrane-based metamaterials. *Appl Phys Lett* 2015; **106**: 051901.
123. Ambati M, Fang N and Sun C *et al.* Surface resonant states and superlensing in acoustic metamaterials. *Phys Rev B* 2007; **75**: 195447.
124. Park CM, Park JJ and Lee SH *et al.* Amplification of acoustic evanescent waves using metamaterial slabs. *Phys Rev Lett* 2011; **107**: 194301.
125. Zhu J, Christensen J and Jung J *et al.* A holey-structured metamaterial for acoustic deep-subwavelength imaging. *Nat Phys* 2011; **7**: 52–5.
126. Jia H, Ke MZ and Hao R *et al.* Subwavelength imaging by a simple planar acoustic superlens. *Appl Phys Lett* 2010; **97**: 173507.
127. Molerón M and Daraio C. Acoustic metamaterial for subwavelength edge detection. *Nat Commun* 2015; **6**: 8037.
128. Li J, Fok L and Yin XB *et al.* Experimental demonstration of an acoustic magnifying hyperlens. *Nat Mater* 2009; **8**: 931–4.
129. García-Chocano VM, Christensen J and Sánchez-Dehesa J. Negative refraction and energy funneling by hyperbolic materials: an experimental demonstration in acoustics. *Phys Rev Lett* 2014; **112**: 144301.
130. Shen C, Xie YB and Sui N *et al.* Broadband acoustic hyperbolic metamaterial. *Phys Rev Lett* 2015; **115**: 254301.
131. Lemoult F, Fink M and Lerosey G. Acoustic resonators for far-field control of sound on a subwavelength scale. *Phys Rev Lett* 2011; **107**: 064301.
132. Pendry JB, Schurig D and Smith DR. Controlling electromagnetic fields. *Science* 2006; **312**: 1780–2.
133. Leonhardt U. Optical conformal mapping. *Science* 2006; **312**: 1777–80.
134. Chen HY, Chan CT and Sheng P. Transformation optics and metamaterials. *Nat Mater* 2010; **9**: 387–96.
135. Graeme WM, Marc B and John RW. On cloaking for elasticity and physical equations with a transformation invariant form. *New J Phys* 2006; **8**: 248.
136. Steven AC and David S. One path to acoustic cloaking. *New J Phys* 2007; **9**: 45.
137. Chen HY and Chan CT. Acoustic cloaking in three dimensions using acoustic metamaterials. *Appl Phys Lett* 2007; **91**: 183518.
138. Cummer SA, Popa B-I and Schurig D *et al.* Scattering theory derivation of a 3D acoustic cloaking shell. *Phys Rev Lett* 2008; **100**: 024301.
139. Daniel T and José S-D. Acoustic cloaking in two dimensions: a feasible approach. *New J Phys* 2008; **10**: 063015.
140. Cheng Y, Yang F and Xu JY *et al.* A multilayer structured acoustic cloak with homogeneous isotropic materials. *Appl Phys Lett* 2008; **92**: 151913.
141. Norris AN. Acoustic cloaking theory. *Proc R Soc Lond A* 2008; **464**: 2411–34.
142. Norris AN. Acoustic metafluids. *J Acoust Soc Am* 2009; **125**: 839–49.
143. Milton GW and Cherkaev AV. Which elasticity tensors are realizable? *J Eng Mater Technol* 1995; **117**: 483–93.
144. Kadic M, Bückmann T and Stenger N *et al.* On the practicability of pentamode mechanical metamaterials. *Appl Phys Lett* 2012; **100**: 191901.
145. Layman CN, Naify CJ and Martin TP *et al.* Highly anisotropic elements for acoustic pentamode applications. *Phys Rev Lett* 2013; **111**: 024302.
146. Chen Y, Zheng MY and Liu XN *et al.* Broadband solid cloak for underwater acoustics. *Phys Rev B* 2017; **95**: 180104.
147. Zhang S, Xia CG and Fang N. Broadband acoustic cloak for ultrasound waves. *Phys Rev Lett* 2011; **106**: 024301.
148. Li J and Pendry JB. Hiding under the carpet: a new strategy for cloaking. *Phys Rev Lett* 2008; **101**: 203901.
149. Popa B-I, Zigoneanu L and Cummer SA. Experimental acoustic ground cloak in air. *Phys Rev Lett* 2011; **106**: 253901.
150. Zigoneanu L, Popa B-I and Cummer SA. Three-dimensional broadband omnidirectional acoustic ground cloak. *Nat Mater* 2014; **13**: 352–5.
151. Bi YF, Jia H and Lu WJ *et al.* Design and demonstration of an underwater acoustic carpet cloak. *Sci Rep* 2017; **7**: 705.
152. Lai Y, Ng J and Chen HY *et al.* Illusion optics: the optical transformation of an object into another object. *Phys Rev Lett* 2009; **102**: 253902.
153. Kan WW, Liang B and Zhu XF *et al.* Acoustic illusion near boundaries of arbitrary curved geometry. *Sci Rep* 2013; **3**: 1427.
154. Shen C, Xu J and Fang NX *et al.* Anisotropic complementary acoustic metamaterial for canceling out aberrating layers. *Phys Rev X* 2014; **4**: 041033.
155. Zhu RR, Ma C and Zheng B *et al.* Bifunctional acoustic metamaterial lens designed with coordinate transformation. *Appl Phys Lett* 2017; **110**: 113503.
156. Zhang P, Li TC and Zhu J *et al.* Generation of acoustic self-bending and bottle beams by phase engineering. *Nat Commun* 2014; **5**: 4316.
157. Shi CZ, Dubois M and Wang Y *et al.* High-speed acoustic communication by multiplexing orbital angular momentum. *Proc Natl Acad Sci USA* 2017; **114**: 7250–3.
158. Marzo A, Seah SA and Drinkwater BW *et al.* Holographic acoustic elements for manipulation of levitated objects. *Nat Commun* 2015; **6**: 8661.
159. Li Y, Liang B and Gu ZM *et al.* Reflected wavefront manipulation based on ultrathin planar acoustic metasurfaces. *Sci Rep* 2013; **3**: 2546.

160. Li Y, Jiang X and Li RQ *et al.* Experimental realization of full control of reflected waves with subwavelength acoustic metasurfaces. *Phys Rev Appl* 2014; **2**: 064002.
161. Xie YB, Wang WQ and Chen HY *et al.* Wavefront modulation and subwavelength diffractive acoustics with an acoustic metasurface. *Nat Commun* 2014; **5**: 5553.
162. Tang K, Qiu CY and Ke MZ *et al.* Anomalous refraction of airborne sound through ultrathin metasurfaces. *Sci Rep* 2015; **4**: 6517.
163. Ma GC, Yang M and Xiao SW *et al.* Acoustic metasurface with hybrid resonances. *Nat Mater* 2014; **13**: 873–8.
164. Li Y, Jiang X and Liang B *et al.* Metascreen-based acoustic passive phased array. *Phys Rev Appl* 2015; **4**: 024003.
165. Cheng Y, Zhou C and Yuan BG *et al.* Ultra-sparse metasurface for high reflection of low-frequency sound based on artificial Mie resonances. *Nat Mater* 2015; **14**: 1013–9.
166. Jiang X, Li Y and Liang B *et al.* Convert acoustic resonances to orbital angular momentum. *Phys Rev Lett* 2016; **117**: 034301.
167. Ye LP, Qiu CY and Lu JY *et al.* Making sound vortices by metasurfaces. *AIP Adv* 2016; **6**: 085007.
168. Zhu YF, Fan XD and Liang B *et al.* Ultrathin acoustic metasurface-based Schroeder diffuser. *Phys Rev X* 2017; **7**: 021034.
169. Xie BY, Tang K and Cheng H *et al.* Coding acoustic metasurfaces. *Adv Mater* 2017; **29**: 1603507.
170. Li Y, Shen C and Xie YB *et al.* Tunable asymmetric transmission via lossy acoustic metasurfaces. *Phys Rev Lett* 2017; **119**: 035501.
171. Melde K, Mark AG and Qiu T *et al.* Holograms for acoustics. *Nature* 2016; **537**: 518–22.
172. Xie YB, Shen C and Wang WQ *et al.* Acoustic holographic rendering with two-dimensional metamaterial-based passive phased array. *Sci Rep* 2016; **6**: 35437.
173. Yang M and Sheng P. Sound absorption structures: from porous media to acoustic metamaterials. *Annu Rev Mater Res* 2017; **47**: 83–114.
174. Mei J, Ma GC and Yang M *et al.* Dark acoustic metamaterials as super absorbers for low-frequency sound. *Nat Commun* 2012; **3**: 756.
175. Yang M, Li Y and Meng C *et al.* Sound absorption by subwavelength membrane structures: a geometric perspective. *Compt Rendus Mec* 2015; **343**: 635–44.
176. Merkel A, Theocharis G and Richoux O *et al.* Control of acoustic absorption in one-dimensional scattering by resonant scatterers. *Appl Phys Lett* 2015; **107**: 244102.
177. Leroy V, Strybulevych A and Lanoy M *et al.* Superabsorption of acoustic waves with bubble metascreens. *Phys Rev B* 2015; **91**: 020301.
178. Chong YD, Ge L and Cao H *et al.* Coherent perfect absorbers: time-reversed lasers. *Phys Rev Lett* 2010; **105**: 053901.
179. Bliokh KY, Bliokh YP and Freilikher V *et al. Colloquium*: Unusual resonators: plasmonics, metamaterials, and random media. *Rev Mod Phys* 2008; **80**: 1201–13.
180. Wei PJ, Croënne C and Tak Chu S *et al.* Symmetrical and anti-symmetrical coherent perfect absorption for acoustic waves. *Appl Phys Lett* 2014; **104**: 121902.
181. Yang M, Ma GC and Yang ZY *et al.* Subwavelength perfect acoustic absorption in membrane-type metamaterials: a geometric perspective. *EPJ Appl Metamater* 2015; **2**: 10.
182. Meng C, Zhang X and Tang ST *et al.* Acoustic coherent perfect absorbers as sensitive null detectors. *Sci Rep* 2017; **7**: 43574.
183. Song JZ, Bai P and Hang ZH *et al.* Acoustic coherent perfect absorbers. *New J Phys* 2014; **16**: 033026.
184. Yang M, Meng C and Fu CX *et al.* Subwavelength total acoustic absorption with degenerate resonators. *Appl Phys Lett* 2015; **107**: 104104.
185. Romero-García V, Theocharis G and Richoux O *et al.* Use of complex frequency plane to design broadband and sub-wavelength absorbers. *J Acoust Soc Am* 2016; **139**: 3395–403.
186. Jiménez N, Huang W and Romero-García V *et al.* Ultra-thin metamaterial for perfect and quasi-omnidirectional sound absorption. *Appl Phys Lett* 2016; **109**: 121902.
187. Groby JP, Duclos A and Dazel O *et al.* Absorption of a rigid frame porous layer with periodic circular inclusions backed by a periodic grating. *J Acoust Soc Am* 2011; **129**: 3035–46.
188. Lagarrigue C, Groby JP and Tournat V *et al.* Absorption of sound by porous layers with embedded periodic arrays of resonant inclusions. *J Acoust Soc Am* 2013; **134**: 4670–80.
189. Groby JP, Lagarrigue C and Brouard B *et al.* Using simple shape three-dimensional rigid inclusions to enhance porous layer absorption. *J Acoust Soc Am* 2014; **136**: 1139–48.
190. Groby JP, Lagarrigue C and Brouard B *et al.* Enhancing the absorption properties of acoustic porous plates by periodically embedding Helmholtz resonators. *J Acoust Soc Am* 2015; **137**: 273–80.
191. Lagarrigue C, Groby JP and Dazel O *et al.* Design of metaporous supercells by genetic algorithm for absorption optimization on a wide frequency band. *Appl Acoust* 2016; **102**: 49–54.
192. Weisser T, Groby JP and Dazel O *et al.* Acoustic behavior of a rigidly backed poroelastic layer with periodic resonant inclusions by a multiple scattering approach. *J Acoust Soc Am* 2016; **139**: 617–29.
193. Fu CX, Zhang XN and Yang M *et al.* Hybrid membrane resonators for multiple frequency asymmetric absorption and reflection in large waveguide. *Appl Phys Lett* 2017; **110**: 021901.
194. Yang M, Chen SY and Fu CX *et al.* Optimal sound-absorbing structures. *Mater Horiz* 2017; **4**: 673–80.
195. Jiménez N, Romero-García V and Pagneux V *et al.* Quasiperfect absorption by subwavelength acoustic panels in transmission using accumulation of resonances due to slow sound. *Phys Rev B* 2017; **95**: 014205.
196. Groby JP, Pommier R and Aurégan Y. Use of slow sound to design perfect and broadband passive sound absorbing materials. *J Acoust Soc Am* 2016; **139**: 1660–71.
197. Jiang X, Liang B and Li RQ *et al.* Ultra-broadband absorption by acoustic metamaterials. *Appl Phys Lett* 2014; **105**: 243505.
198. Bender CM and Boettcher S. Real spectra in non-Hermitian Hamiltonians having PT symmetry. *Phys Rev Lett* 1998; **80**: 5243–6.
199. Feng L, Xu YL and Fegadolli WS *et al.* Experimental demonstration of a unidirectional reflectionless parity-time metamaterial at optical frequencies. *Nat Mater* 2012; **12**: 108–13.
200. Chong YD, Ge L and Stone AD. PT-symmetry breaking and laser-absorber modes in optical scattering systems. *Phys Rev Lett* 2011; **106**: 093902.
201. Chang L, Jiang XS and Hua SY *et al.* Parity–time symmetry and variable optical isolation in active–passive-coupled microresonators. *Nat Photon* 2014; **8**: 524–9.
202. Feng L, Wong ZJ and Ma RM *et al.* Single-mode laser by parity-time symmetry breaking. *Science* 2014; **346**: 972–5.
203. Fleury R, Sounas DL and Alù A. Parity-time symmetry in acoustics: theory, devices, and potential applications. *IEEE J Select Topics Quantum Electron* 2016; **22**: 121–9.

204. Shi CZ, Dubois M and Chen Y *et al.* Accessing the exceptional points of parity-time symmetric acoustics. *Nat Commun* 2016; **7**: 11110.
205. Christensen J, Willatzen M and Velasco VR *et al.* Parity-time synthetic phononic media. *Phys Rev Lett* 2016; **116**: 207601.
206. Aurégan Y and Pagneux V. PT-symmetric scattering in flow duct acoustics. *Phys Rev Lett* 2017; **118**: 174301.
207. Ding K, Ma GC and Xiao M *et al.* Emergence, coalescence, and topological properties of multiple exceptional points and their experimental realization. *Phys Rev X* 2016; **6**: 021007.
208. Lai Y, Wu Y and Sheng P *et al.* Hybrid elastic solids. *Nat Mater* 2011; **10**: 620–4.
209. Zheng X, Lee H and Weisgraber TH *et al.* Ultralight, ultrastiff mechanical metamaterials. *Science* 2014; **344**: 1373–7.
210. Christensen J, Kadic M and Kraft O *et al.* Vibrant times for mechanical metamaterials. *MRS Commun* 2015; **5**: 453–62.
211. Popa B-I, Zigoneanu L and Cummer SA. Tunable active acoustic metamaterials. *Phys Rev B* 2013; **88**: 024303.
212. Popa B-I and Cummer SA. Non-reciprocal and highly nonlinear active acoustic metamaterials. *Nat Commun* 2014; **5**: 3398.
213. Pennec Y, Laude V and Papanikolaou N *et al.* Modeling light-sound interaction in nanoscale cavities and waveguides. *Nanophotonics* 2014; **3**: 413–40.
214. Maldovan M. Sound and heat revolutions in phononics. *Nature* 2013; **503**: 209–17.
215. Chu Y, Kharel P and Renninger WH *et al.* Quantum acoustics with superconducting qubits. *Science* 2017; **358**: 199–202.
216. Yu SY, He C and Wang Z *et al.* A monolithic topologically protected phononic circuit. 2017, arXiv:1707.04901.